Department of Precision and Microsystems Engineering

Inkjet printing of a low actuation voltage dielectric elastomer actuator

S. A. M. Elschot

Report no : 2021.042
Supervisor : Dr. ir. M. Tichem
Specialisation : Micro and Nano Engineering
Type of report : Master thesis
Date : July 23, 2021

TU Delft Delft University of Technology

Challenge the future

Inkjet printing of a low actuation voltage dielectric elastomer actuator

by

S.A.M. Elschot

to obtain the degree of Master of Science

at the Delft University of Technology,

to be defended publicly on Friday July 23, 2021 at 13:30 PM.

Student number:	4270517	
Project duration:	July 24, 2020 – July 23, 2021	
Thesis committee:	Dr. ir. M. Tichem,	TU Delft, supervisor
	Dr. A. Hunt,	TU Delft
	Dr.ir. J. F. L. Goosen,	TU Delft

An electronic version of this thesis is available at `http://repository.tudelft.nl/`.

TU Delft

Acknowledgements

During this thesis I've learned all about a specific part of the micro- and nano engineering world, but at the same time I've learned more about myself than I could have imagined when the project started. Before taking the reader into the outcome of my year of research, I'd like to thank several people who have been there with me along the way.

First I'd like to thank Marcel Tichem, my supervisor, for the brainstorming and guidance, while still leaving me free to choose the best next step in the project. The 3mE lab technicians for their support during the experiments. Andres Hunt, for sharing ideas on printing, the printer repairs and helping with the laser experiments. Ron van Ostayen, for taking the time to go through the COMSOL model with me and giving crucial tips. Yavuz Emre Kamış for the help with the viscosity and surface tension measurements.

Besides the staff supporting this research, I've also been lucky enough to have had friends and family tolerating me while thinking out loud and venting my frustrations whenever it was necessary. I'd like to thank Irene, Dianne and Marlo in particular for dragging me over the finish line these last months. Abel, for all the constructive feedback but mostly for simply being there. And last but not least, I want to thank Karin, Emiel, Marije and Puck for continuing to lift me up during my time here in Delft.

"Ik heb het nog nooit gedaan, dus ik denk dat ik het wel kan"

Sanne
Delft, July 2021

Abstract

Dielectric elastomer actuators (DEAs) are a type of soft actuators that consist of a dielectric elastomer membrane, covered with an electrode on the top and the bottom. When applying a potential, the opposite charges on the electrodes induce an electrostatic force which squeezes the elastomer, causing it to expand. This expansion can be used as an actuation mechanism, in a wide variety of applications. A specific field of interest are low actuation voltage DEAs. These DEAs require low stiffness and thin elastomer layers, but are easier and cheaper to implement due to the lower voltage requirements.

The goal of this research is to develop a manufacturing process for an inkjet printed low actuation voltage DEA, while achieving insights into the requirements and limitations of the steps involved with this process.

By using the PiXDRO LP50 inkjet printer in combination with the Dimatix DMC printhead, the bottom electrode is printed on a Novele substrate with Mitsubishi NBSIJ-MU01 AgNP ink. A dielectric elastomer ink has been formulated consisting of polydimethylsiloxane (PDMS) and octyl acetate (OA) in 1:4 and 1:3 ratios. These inks have been characterised on several printability parameters, placing both formulations in the jettable range with Z = 1.396 for PDMS:OA 1:3 and Z = 2.374 for PDMS:OA 1:4. Although theoretically jettable, both formulations showed difficult jetting behaviour. To resume the research, the PDMS layer is instead applied by spin coating.

The PDMS surface is hydrophobic, requiring surface treatment before the electrode can be printed on top. Several methods have been investigated, of which O_2 plasma treatment showed the best results. The top electrode is printed using NovaCentrix Metalon JS-B25P AgNP ink. The printed silver electrode could not be thermally cured and showed limited success when using an out-of-focus laser for photonic sintering. Next to the experimental work, a finite element analysis model has been built to provide a basis for designing low actuation voltage DEAs. The model has been validated using measurement data by Poulin et al. [1]

Contents

1 Introduction

This Masters thesis describes the research into using an inkjet printer to manufacture a dielectric elastomer actuator (DEA). DEAs are soft actuators that change shape when an electric field is applied. Due to the electrostatic force induced by opposite charges, the electrodes will compress the elastomer membrane lying in between which causes it to expand, as shown in figure 1.1.

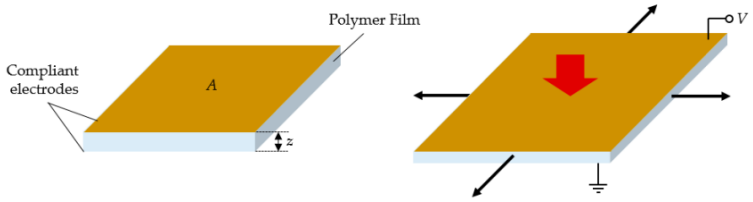

Figure 1.1: General working principle of a dielectric elastomer actuator, taken from [2]

The actuation output can be controlled by restricting the DEA or changing the design in such a way that a certain motion is obtained [3–5]. Figure 1.2 shows a bistable rotating mechanism created by Liu et al. [6], which channels the expansion of the DEA into flipping a rigid frame, resulting in two stable configurations. Figure 1.3, from the research by Araromi et al. [7], shows a gripper designed as a minimum energy structure that folds inward upon actuation, making it capable of gripping various objects. In both of these examples the expansion of the DEA is converted into a specific motion required for the device's intended purpose.

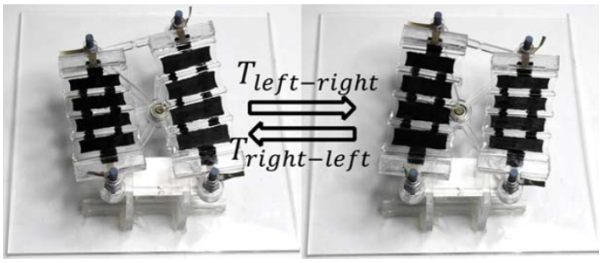

Figure 1.2: Bistable rotating mechanism, the black patches are DEAs which push the mechanism to the other side upon actuation, taken from [6]

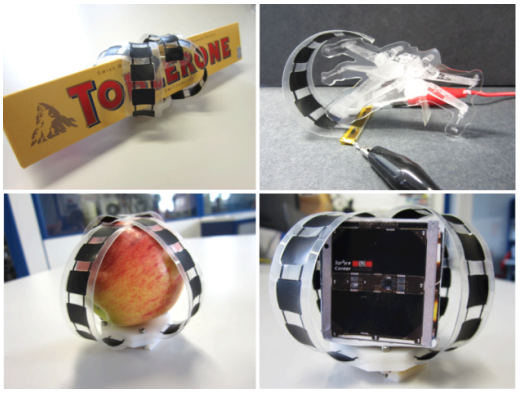

Figure 1.3: Gripper that closes upon actuator, wrapped around various objects, taken from [7]

Often, DEAs in research are created by pre-stretching a dielectric elastomer (such as off-the-shelf 3M VHB 4910 tape [9, 10]) and applying electrodes on the top and bottom [11], sometimes even as coarse as a paste with carbon particles [12].

1.1. Problem statement

In order to be able to implement DEAs in micrometer scaled applications, a more sophisticated manufacturing process is required to produce these small-scale DEAs, which brings us to the problem statement for this thesis. Several established manufacturing methods are currently used in DEA research, which come with

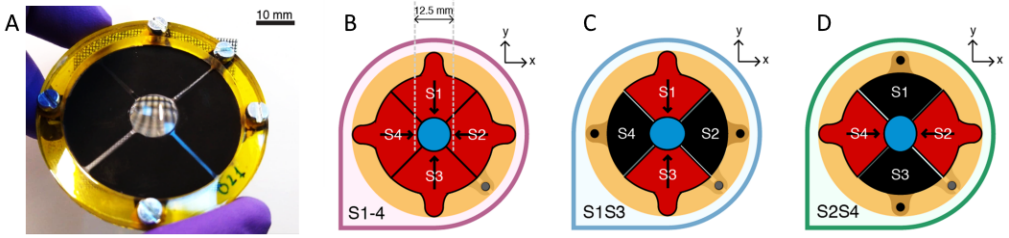

Figure 1.4: A tunable lens, from left to right: A) the prototype, B) activating all four segments causes a radial uniform squeezing, C) activating the first and third segments causes horizontal elongation, D) activating the second and fourth segments causes vertical elongation, adapted from [8]

their own limitations and downsides. Prefabricated elastomer films can be used with automated manufacturing methods to improve reliability and consistency [13], but does not allow for easy miniaturisation of the DEA. Contact-based methods, such as screen printing or nano-imprinting, can damage the fragile elastomer layer, whereas a non-contact method using a mask, such as spraying, has a low resolution which makes small complex designs difficult to manufacture [14]. Additionally, the actuation voltage required to achieve large deformations is strongly linked to the thickness of the dielectric elastomer. With inkjet printing, a dielectric elastomer layer of as thin as 5 μm can be produced with complex design patterning, due to the high level of control with drop-on-demand systems [15–17]. This opens up possibilities for manufacturing low actuation voltage DEAs, which makes them easier to implement outside of experimental settings. Whereas regular DEAs require voltages in the range of kilovolts, a low actuation voltage DEA can operate at voltages as low as 245 V [18]. This opens up more applications for DEAs, as voltages in the kV range come with safety concerns and expensive electronics equipment.

Research goal

The main goal of this research was to develop a manufacturing process for an inkjet printed low actuation voltage DEA, while achieving insights into the requirements and limitations of the steps involved with this process.

Suitable materials had to be found and the interactions between the different components that build the actuator were examined. This involved preparing a dielectric elastomer ink based on PDMS and characterising its properties for printability.

The limitations of printing with the PiXDRO LP50 and DMC printhead were investigated, in combination with the materials used to build the DEA.

Next to the experimental work, a finite element analysis (FEA) model of an low actuation voltage DEA has been built, to aid future design choices and predict the behaviour of an actuated DEA.

1.2. Report structure

The results of the conducted research are detailed in this report. The first chapter covers inkjet printing and working with the PiXDRO LP50. (External) factors influencing the print process during the experiments are described, along with directions on improving the inkjet printing process.

The following chapters concern the individual components of the DEA, the materials and methods used and the observations during the experimental processes involved in creating the component.

After the experimental section, the FEA model is described in chapter 7. Finally, the report is concluded with an overview of the obtained results and their discussion, ending with recommendations for future research.

2

Inkjet printing

Inkjet printing is an established manufacturing method for (experimental) soft electronics. Using drop-on-demand technologies in combination with metal nanoparticle inks, high-definition and complex electronics designs can be produced quickly and designs are easily altered. From soft electronics it is a small step to soft actuators. Combining electroactive materials with electrodes creates mechanisms which can be used for a wide variety of applications [19].

During this research, a PiXDRO LP50 inkjet printer (Süss-MicroTec) in combination with a DMC print head assembly (Meyer Burger) and DMC-11610 cartridge (FUJIFILM Dimatix) have been used, as shown in figure 2.1. This chapter provides background information on working with the PiXDRO printer in combination with the DMC Print Head Assembly (PHA), based on existing literature and experimental findings during this thesis.

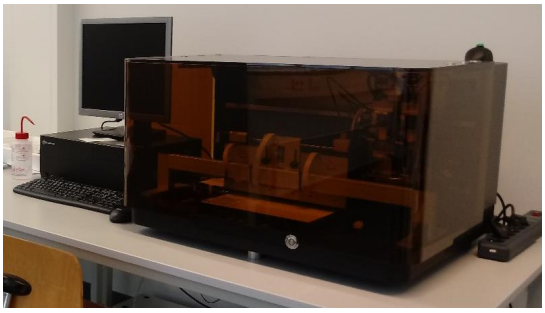

(a) PiXDRO LP50 printer

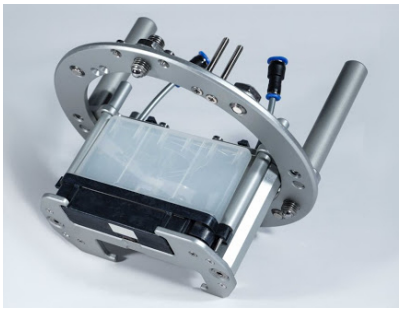

(b) DMC PHA with DMC-11610 cartridge installed, photo by JBI

Figure 2.1: Inkjet print set-up, consisting of (a) the PiXDRO LP50 and (b) the DMC print head assembly containing the cartridge

2.1. Print settings

The PiXDRO LP50 is designed for experimental applications. If desired, it is possible to adjust almost all parameters controlling the printer. This section will expand on several basic settings and their influence on print results.

Print speed

Equation 2.1 links print speed v [mm/s] to the quality factor QF [-], the jetting frequency F [Hz] and resolution R_p [DPI]. The quality factor is defined as the number of nozzles used to print one line in in-scan direction (parallel to print direction). A lower print speed generally produces better quality prints, but will increase print time [20]. Higher jetting frequency prints faster, however low viscosity inks usually perform better at lower frequencies. High viscosity inks are less sensitive and are better suited for high frequency jetting [21]. The print resolution is based on the drop size and drop spacing on the substrate in combination with the desired definition of the print. If the print design contains complex or detailed features, the waveform can be adjusted to produce smaller droplets (see also section 2.2.2) and the resolution should be adapted accordingly.

$$v = \frac{25.4 \times QF \times F}{R_p} \tag{2.1}$$

Print(bed) temperature
The print bed can be heated up to 90 °C, which can be utilized to settle the printed lines by evaporating the solvent or even (pre)cure the ink. When using a high print bed temperature, caution should be taken with the temperature of the print head. Especially with long continuous prints, the print head temperature will rise significantly if the temperature difference with the print bed is large. This will cause the ink properties to change, such as the viscosity, which influences jetting behaviour. If the printhead temperature is fixed at a certain value, going out of this range will cause an error and stops the print. If the temperature in the print head rises high enough to evaporate the solvent, the nozzles can clog (partially) which can ruin the print. Unfortunately, the printer has no cooling functionalities, only heating.

Nozzle selection
Finding the right nozzle(s) to print with starts with a cleaning cycle. Purge the ink, wipe the printhead and check which nozzles work properly using the internal dropviewer. To prevent ink spillage and a mess in general it is best to only activate a selection of nozzles at a time.

Using multiple nozzles will reduce the total printing time, but it is a risk for jetting stability. When inspecting the droplets in dropview, it is often found that the drop volume and velocity is significantly reduced when two or more nozzles are activated. Unless the ink used for printing is very stable or the print design can sacrifice quality for faster printing, multiple nozzles should be used with caution. Next to possible jetting issues, alignment problems have occurred when printing with multiple nozzles. Figure 2.2a shows a print with badly printed vertical areas where the printhead shifted to the next set of swaths due to the offset between the two activated nozzles (#9 and #13, printing in Y-direction). In figure 2.2b the print simulation shows the swaths, with nozzle #9 in blue and nozzle #13 in green. After completing the first set of swaths with both nozzles jetting simultaneously, the printhead moves over a relatively large distance to resume printing, which is prone to small alignment errors and affects the jetting when printing with a difficult ink.

(a) Electrode printed with two nozzles where a vertical line defect has occurred. Captured with the PiXDRO print view camera

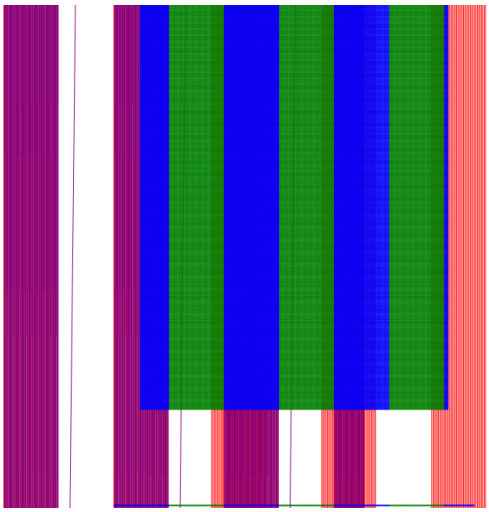

(b) Simulation of print with two nozzles (blue and green), 2 passes. The red and purple lines depict the movement of the print head

Figure 2.2: Print defect due to shift in printhead movement

External factors to consider
External factors can heavily influence the print quality. For example, figure 2.3 shows four different prints, all printed with the same silver ink (Novacentrix NBSIJ-01). The electrodes in figure 2.3a and figure 2.3b were printed on a sunny day (March 1st), whereas during the printing of the electrodes in figure 2.3c and figure 2.3d it was snowing outside (March 6th). The printer used for this research is located next to a window (with automated sunscreen) and a radiator in a regular lab space. All prints were done without a heated printbed, but with a fixed printhead temperature. There is a clear difference in print quality (besides any defects due to the porous membrane substrate), which marks the importance of a controlled lab environment and using the heated printbed for repeatability in manufacturing.

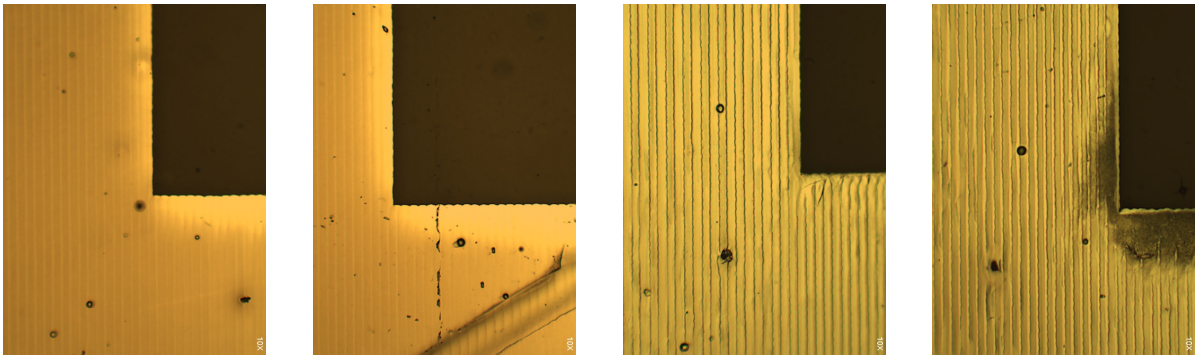

(a) First electrode printed on March 1st

(b) Second electrode printed on March 1st

(c) First electrode printed on March 6th

(d) Second electrode printed on March 6th

Figure 2.3: 10x magnification microscopic images of printed electrodes

2.2. Waveform

The waveform settings sent to the printhead can be adjusted through the PiXDRO Human Machine Interface (HMI). Figure 2.4 shows a screenshot of the HMI software, where the waveform (or pulseshape) is controlled by the voltage (high, middle, low) and the duration of sections 1 to 8. The physical meaning of these different sections are divided into four phases, as shown in fig 2.5.

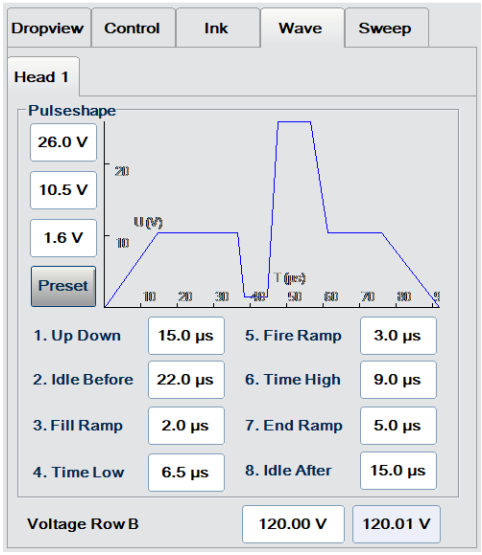

Figure 2.4: Waveform parameters in the PiXDRO HMI

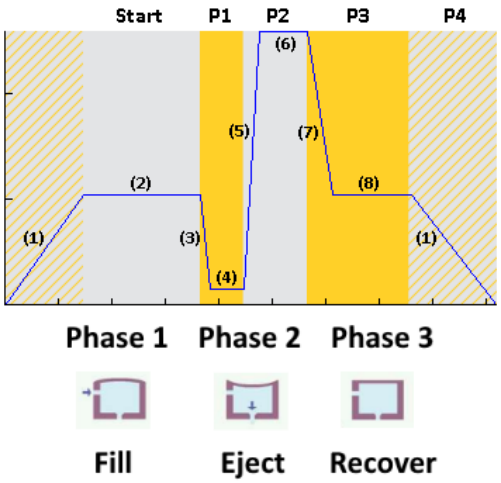

Figure 2.5: Waveform sections indictated between brackets, different phases indicated by alternating colors

2.2.1. Actuation phases

The bottom voltage limit of the waveform is fixed to zero, due to a physical limitation of the electronics. Thus, section 1 starts at 0 volt and rises to V_{mid}, where it remains for a period of time set by section 2. Because the printhead is not capable of negative voltages, the start of the actuation is set at V_{mid}. "Start" indicates the standby position of the piezo element, where the fluid in the chamber is at rest under a bias voltage of V_{mid}. In phase 1, the voltage drops to V_{low} with a speed determined by the fill ramp duration (section 3) and remains there for the duration of section 4 to fill the ink chamber. Phase 2 is where the droplet is ejected: the ink chamber is compressed with a force defined by the steepness (also called "slew rate") of section 5, the duration of section 6 and V_{max} which causes the ink to be pressed out of the nozzle. Phase 3 is the recovery phase; the piezo element returns to the bias voltage V_{mid} and the fluid inside the chamber is retracted, causing the droplet to pinch off and be jetted. In phase 4, the voltage level returns to zero and the print cycle starts again.

2.2.2. Tuning the waveform

Several studies have been done into designing waveforms using material parameters [22, 23]. However, without knowing all specifications of the printer and printhead, obtaining a working waveform remains a trial-and-error process.

To adjust the waveform to accommodate different inks, a few guidelines can be followed. The waveform provided by Dimatix for the DMP-11610 cartridge serves as a starting point. In general, inks with higher viscosities perform better at higher jetting frequencies and require higher jetting voltages to attain the same velocity as a lower viscosity fluid.

Once a working waveform has been established, it can be adjusted even further to increase the velocity of the droplet or for troubleshooting. For example, changing ink levels or printhead temperature settings can cause satellite droplets or other unstable jetting performance to occur. In table 2.1, the section adjustments and their effects are listed, as described by [24]. Jetting velocity can be increased by pushing these values to their limits, until tails or satellite droplets are observed or no droplets are formed at all, and then going back to the settings that produce a good droplet. The volume of the droplet is dependent on the applied voltage, as this is directly related to the chamber volume [24].

Table 2.1: Influence of waveform sections on drop velocity, adapted from [24]

Phase	**Section**	**Adjustment**	**Velocity**	**Possible side effects**
1	3	Slew rate down	Faster	Tails
1	4	Shorter duration	Faster	Tails
2	5	Slew rate down	Faster	Tails
3	7	Slew rate up	Faster	-
4	1	Slew rate up	Faster	-

When troubleshooting undesired jetting behaviour table 2.1 can be used in reverse. If satellite droplets are observed, adjust parameters 3, 4 and 5 slightly. However, it should be noted that if the satellite droplet is faster than the main droplet, it can increase the main droplet's velocity when merging. The DMC printhead prints at a fixed distance above the substrate, so the presence of tails can be beneficial as long as the drops merge completely and become stable before they reach the substrate.

3

Substrate

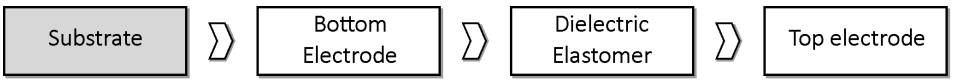

Figure 3.1: Location of the substrate in the DEA structure

The substrate is the foundation of the entire manufacturing process, as shown in figure 3.1. All subsequent material layers will be deposited on top of the substrate, also known as bottom-up fabrication.

3.1. Material

The substrate used in this research is the Novele IJ-220 substrate, which is designed for printed electronics. The substrate consists of a PET sheet coated with a porous membrane [25]. This porous membrane acts as a receptive layer for the printed AgNP ink. This prevents the droplets from spreading after being printed and speeds up curing. When used in combination with certain inks, for example the AgNP inks in this thesis, it has the added benefit of sintering the ink without further requiring post-processing. This behaviour is further expanded on in section 4.1.

3.2. Drawbacks

The Novele substrate comes with certain drawbacks, general flaws which affect any process and specific problems arising when using this substrate in dielectric elastomer actuator fabrication.

3.2.1. General

The substrate comes in A4-sized sheets, which are flexible and very static. This causes the substrate to attract dust and other particles from its surroundings, which adhere to the porous membrane. These particles will cause imperfections in the prints, as shown in figure 3.2.

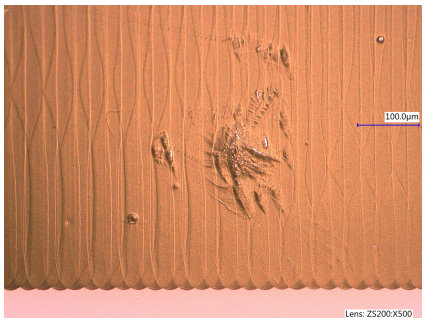

Figure 3.2: Mitsubishi NBSIJ-MU01 printed over a dust particle on the substrate

When handling the sheet of Novele, special care should be taken to ensure the substrate lies flat and does not bend. The PET layer in the substrate can form creases which causes deformities. This is especially evident when cutting the sheet, as shown in figure 3.3. These cracks can propagate further into the sheet if not handled properly.

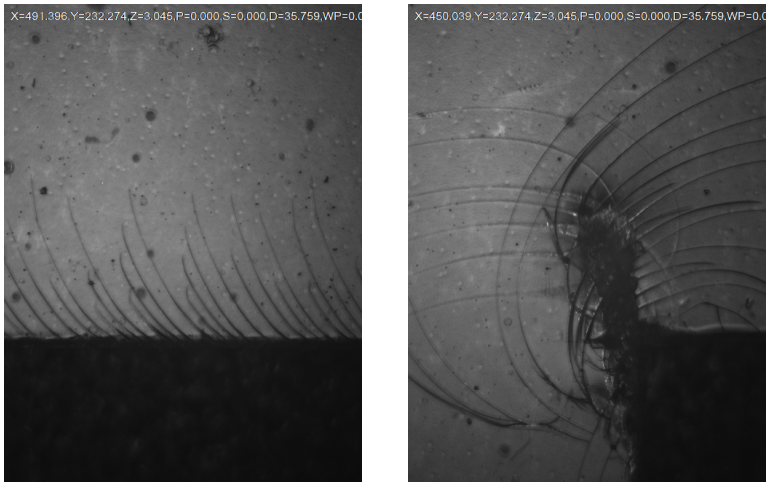

(a) Cracking along cut line (b) Cracking in corner of cut substrate

Figure 3.3: Damaged Novele substrate (in grey) due to cutting with scissors, captured with PiXDRO print view camera

3.2.2. DEA-specific

Because the substrate functions as the foundation of the actuator, its stiffness has impact on the overall actuation performance. The Novele substrate is 140 μm thick [25], which is relatively thick compared to the other layers in the actuator (see section 4.3 and section 5.3). This means that using the Novele as a substrate will severely limit the actuation output. During this research, the focus lies on the manufacturing process instead of the performance of the resulting device, but it is an important factor to consider when producing a DEA. Solutions can be found in other substrate materials, or for example by using a sacrificial layer between a substrate and bottom electrode such as a microscope glass with a poly(vinyl alcohol) coating [26].

4

Bottom electrode

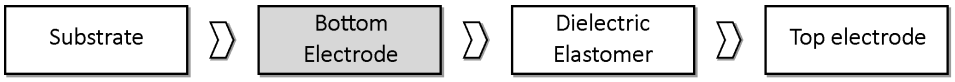

Figure 4.1: Location of the bottom electrode in the DEA structure

The bottom electrode is printed directly on top of the substrate, as depicted in figure 4.1. After printing, the electrode will be covered by the dielectric elastomer, which is discussed in the next chapter. This chapter mainly focuses on the process of printing with Mitsubishi NBSIJ-MU01 silver nanoparticle ink, which has been used for the bottom electrode during this research.

4.1. Materials

The bottom electrode is printed with silver nanoparticle inkjet ink NBSIJ-MU01 (Mitsubishi Paper Mills Limited [27]) on a sheet of Novele IJ-220 (Novacentrix [25]) substrate. This combination was recommended (by Andres Hunt) due to its self-sintering properties and ease of jetting.

The self-sintering aspect of the NBSIJ-MU01 ink requires a substrate with a porous membrane containing certain chemicals which instantly sinter the ink in place [28]. Figure 4.2 depicts the chemical sintering process: (1) shows the printed droplet containing the silver nanoparticles on top of the substrate, followed by (2) the diffusion of chemical sintering agents from the porous membrane and which in step (3) reacts with the dispersing agent, resulting in (4) fused silver particles creating the electrode.

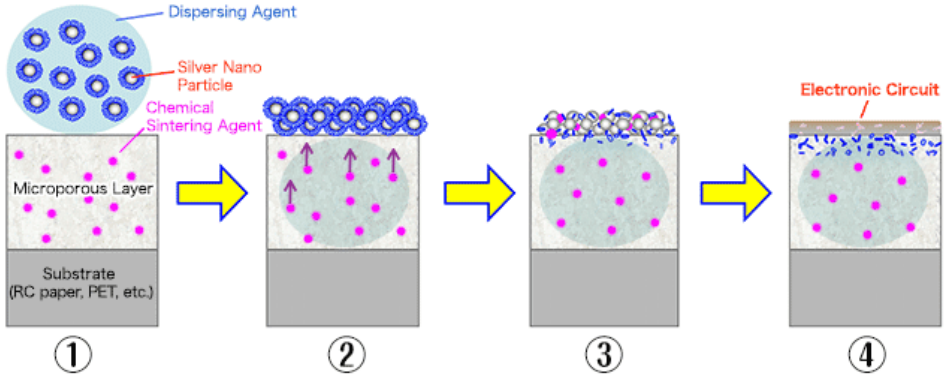

Figure 4.2: Schematic depicting the interactions between NBSIJ-01 ink and the substrate, from [28]

4.2. Design

The bottom electrode is the first step in defining the shape or design of the actuator. In theory, the possibilities are almost endless due to the flexibility of printing with a drop-on-demand system such as the PiXDRO printer. Several interesting studies are working towards more compliant electrodes to increase the actuation output of the DEAs. In these studies, different compliant electrode designs have been proposed, such as patterning the electrode in waves [29, 30], creating a corrugated surface [31] or using the crumpling of the metal which occurs due to different thermal expansion coefficients [32] for example. These methods all increase

the surface area of the electrode, with respect to the dielectric elastomer, which increases the total flexibility of the system. In this research, the focus lies on the process of manufacturing, more so than the design of the actuator. Thus, a simple rectangular electrode shape has been chosen for the bottom electrode, to accommodate fast(er) printing for more experimentation with the process itself. Figure 4.3 shows an example, with a long rectangular block for the electrode, a thinner strip of silver towards the contact pad at the top, which is large enough to attach leads to a power source for actuation. The triangles in each corner are used for alignment, to locate the correct placement for the following layers. The triangular marker has been chosen as it indicates the corners of the print area, as opposed to a circular or cross shaped marker. This provides a quick confirmation of the current position when locating the marker with the built-in camera.

Figure 4.3: Bottom electrode design example

4.3. Printing

The NBSIJ-MU01 ink can be injected directly into the DMC cartridge, without any preparation steps. The general settings used for experiments with this ink can be found in table 4.1. The print bed heating can also be used, but it is not a requirement for drying or curing this silver ink.

Waveform

The base waveform for the Mitsubishi ink can be found in figure 4.4. Prints with the Mitsubishi ink have been performed with that waveform or a slight adaptation to the shape, depending on specific conditions during that print. See also section 2.2.2 for more information.

Table 4.1: Print settings for Mitsubishi NBSIJ-MU01 on Novele

Setting	Value
Print head temperature	25 °C
Print speed	63.5 mm/s
Resolution	1000 DPI
Jetting frequency	1970 Hz
Back pressure	-5 bar

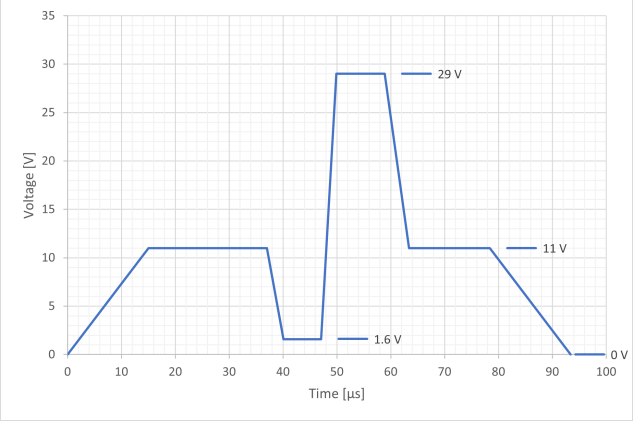

Figure 4.4: Base waveform for Mitsubishi NBSIJ-MU01

Effect of print direction and multiple passes

Figure 4.5 shows prints in varying print direction (see appendix A.1 for a larger version). Each direction is printed in one (1P), two (2P) or three (3P) print passes, with every pass adding another layer of silver of the same image. All rectangles are 50 by 88 pixels printed at a resolution of 1000 DPI. Both print directions (X and Y unilateral) are comparable in resulting print quality, but can heavily differ in print duration depending on (the orientation of) the design. Figure 4.6 shows close-ups of the text printed in both directions. Comparing the letter "i" in both prints, the sharpest line at this resolution is obtained by printing in horizontal direction. Vice versa, printing in vertical direction gives the sharpest horizontal line. Lowering the resolution would benefit the "crispness" of the printed text and other designs with a high level of detail. For the rectangular electrodes however, the high resolution ensures good coverage even with a single pass and is thus better suited for this research.

When examining the single pass prints in figure 4.5, it might seem as if the print is scattered with holes. However, when comparing the same rectangle in different light settings in figure 4.7, it can be seen that the

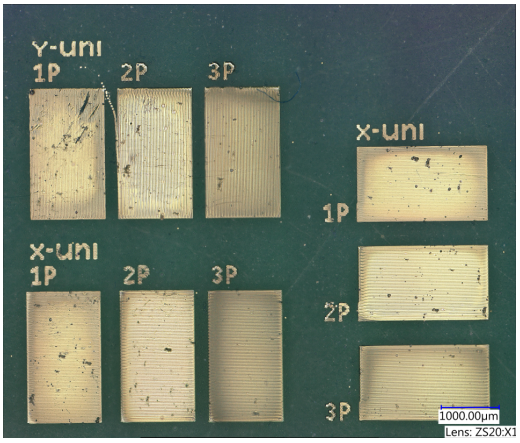

Figure 4.5: Mitsubishi NBSIJ-01 printed on top of Novele IJ-220. Overview of prints with different print directions

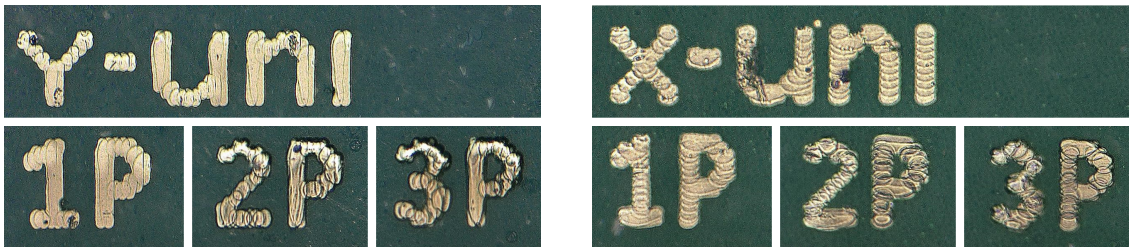

(a) Y-unidirectional print

(b) X-unidirectional print

Figure 4.6: Close-up of printed text

black spots in 4.7a correspond to silver dots in 4.7b. This is probably due to a defective nozzle leaking silver droplets while printing the other rectangles, or a nozzle that is still jetting while examining the finished print. The two largest black spots are damages due to touching the electrode with multimeter probes, to check for conduction. All these prints were conducting immediately upon finishing the print. While the porous membrane of the substrate has no effect on the final print, the underlying PET sheet does. The effect of cracks in this PET layer are visible in the single pass Y-unidirectional print.

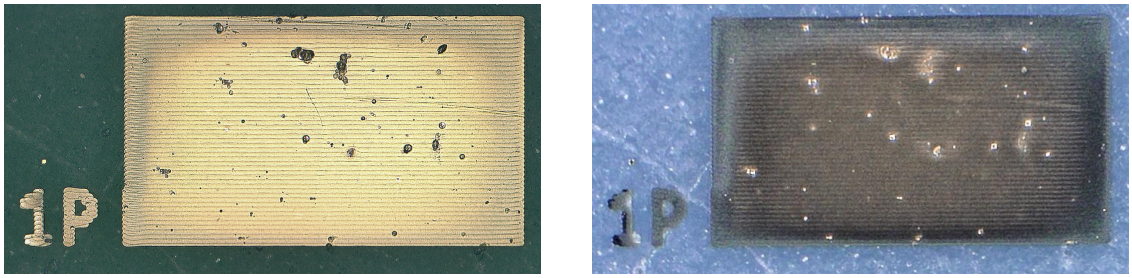

(a) Microscopic image with mixed lighting, 150x magnification

(b) Microscopic image with full ring lighting, 50x magnification

Figure 4.7: Microscopic images of the single pass X-unidirectional horizontal rectangle

Thickness of printed silver

Using a white light interferometer (Bruker) it is possible to determine the approximate layer thickness of the printed silver. Figure 4.8 shows a 3D image of a single pass print in unilateral x-direction. Due to the transparent and porous nature of the substrate it is difficult to perform a sharp measurement of the entire surface. However, when comparing measurements of the single pass x-direction print with the two- and three pass prints a relative added height difference of roughly 0.3 μm can be derived. See appendix B for more detailed images of the measurement results.

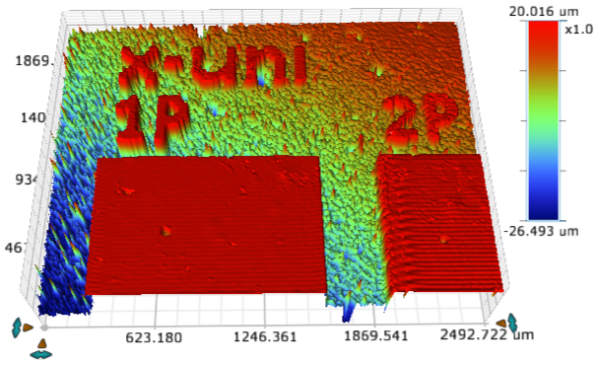

Figure 4.8: Surface topography of the single pass x-direction print

4.4. Post-processing

Due to the self-sintering property of the NBSIJ-MU01 ink when printed on the Novele substrate, no post-processing step is necessary. When the print is finished, the ink is dried and the silver electrode is conducting. Several examples of lowering the sheet resistivity of the printed silver exist in literature, usually by thermally curing the print [33]. For this research, no additional curing steps have been applied.

Contact pad shield

Before applying the dielectric layer, it is important to ensure clear access to the contact pad of the electrode to connect to a power source. A simple yet effective method has been found in low-stick scotch tape. Photo's of the results can be found in appendix C, where figures C.1 to C.2 show the same printed electrode before applying tape, with the tape in place and after removing the tape. Some glue remains on the silver after removal, but the electrode is not damaged. After applying the elastomer layer (see chapter 5), the tape can be easily removed after curing the PDMS, especially when lightly tracing the PDMS on top of the tape with a knife.

5
Dielectric elastomer

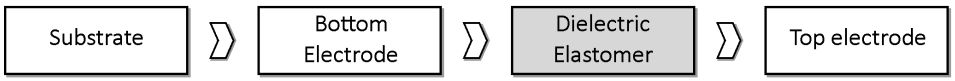

Figure 5.1: Location of the dielectric elastomer in the DEA structure

According to the research by Mikkonen et al. [16], the solution of PDMS with octyl acetate (OA) with a PDMS:OA ratio of 1:3 produces a stable ink for printing. To determine which formulation would be the best fit for this research, formulations with a PDMS:OA ratio of 1:3 and 1:4 have been prepared and tested.

5.1. Materials

First, PDMS (Sylgard 184, Dow Corning [34]) is prepared in a 10:1 base-catalyst ratio following manufacturer's instructions. After stirring the base and catalyst for approximately 5 minutes, the octyl acetate (Sigma Aldrich [35]) is added to the preferred ratio. This mixture is stirred for 15 minutes using a magnetic stirring rod on a mixing plate, to ensure the components mix well. Then, the ink is transferred into a storage flask and ready to be injected into the cartridge for use in the printer.

5.1.1. Characterisation

In order for the ink to be printable, its properties need to meet certain values. A summary of these properties and their ideal ranges is given in table 5.1. The prepared formulations have been tested on these properties, as detailed in the following subsections.

Table 5.1: Summary of ink properties affecting jettability

Property	**Ideal range**
Particle size	< 10% of nozzle diameter [36]
Viscosity	< 20 cP [37]
Surface tension	< 40 mN/m
Z-value	$1 < Z < 10$ [38, 39]

Viscosity

Viscosity plays an important role in jetting the elastomer onto a substrate. When the ink is too viscous it cannot pass through the nozzle, not viscous enough causes the ink to drip out of the print head. The ideal viscosity lies below 20 centipoise, which equals 2 mPa·s (comparable to the viscosity of whole milk) [37]. The viscosity of the PDMS:OA ink formulations has been determined using the MCR 302 rheometer (Anton Paar). The result of the measurements at a constant temperature of 30°C are given in figures 5.2 and 5.3. The tested samples are indicated with their formulation ratio, formulation date (in brackets) and the measurement date. The PDMS:OA 1:4 sample has been tested twice on December 8th, to verify the high viscosity on the first run. When comparing the measurement results of the formulations made on November 11th, both the 1:3 and 1:4 ink formulations show a significant rise in viscosity in the 26 days after preparation.

The temperature dependency of the viscosity is shown in figure 5.4. Because the viscosity reduces when the temperature of the fluid rises, it is possible to achieve better jetting results by adjusting the printhead temperature (within the thermal limits of the printhead and the solvent). As shown in figure 5.2 and 5.3, the viscosity of the inks rises over time, so the printhead temperature needs to be adjusted accordingly.

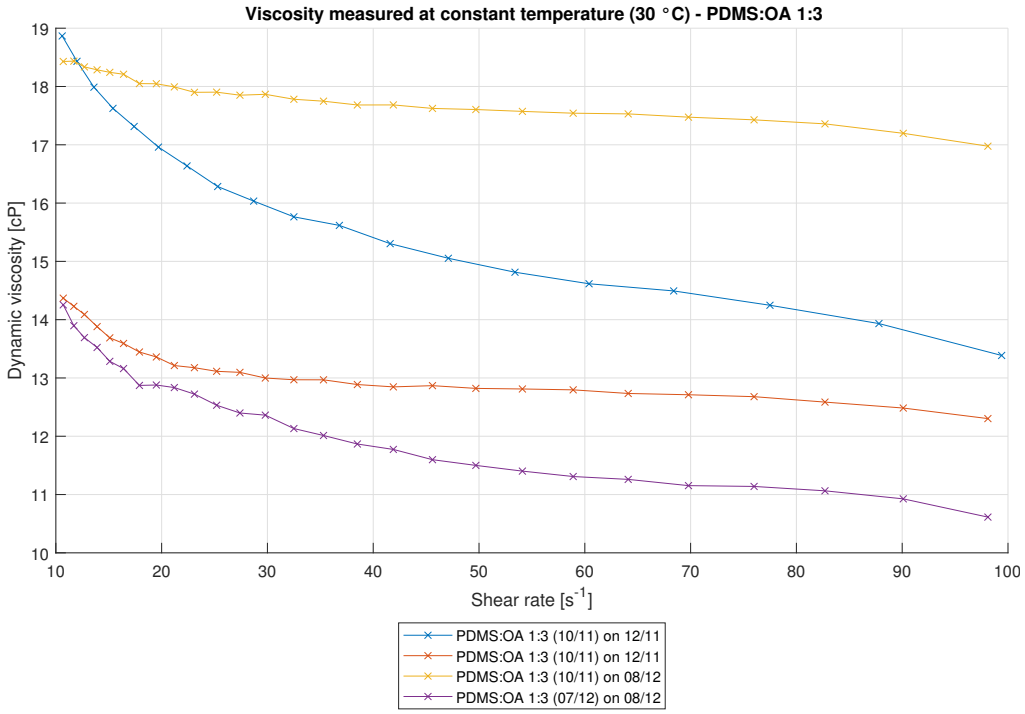

Figure 5.2: Viscosity measurements at a constant temperature of 30°C of PDMS:OA 1:3

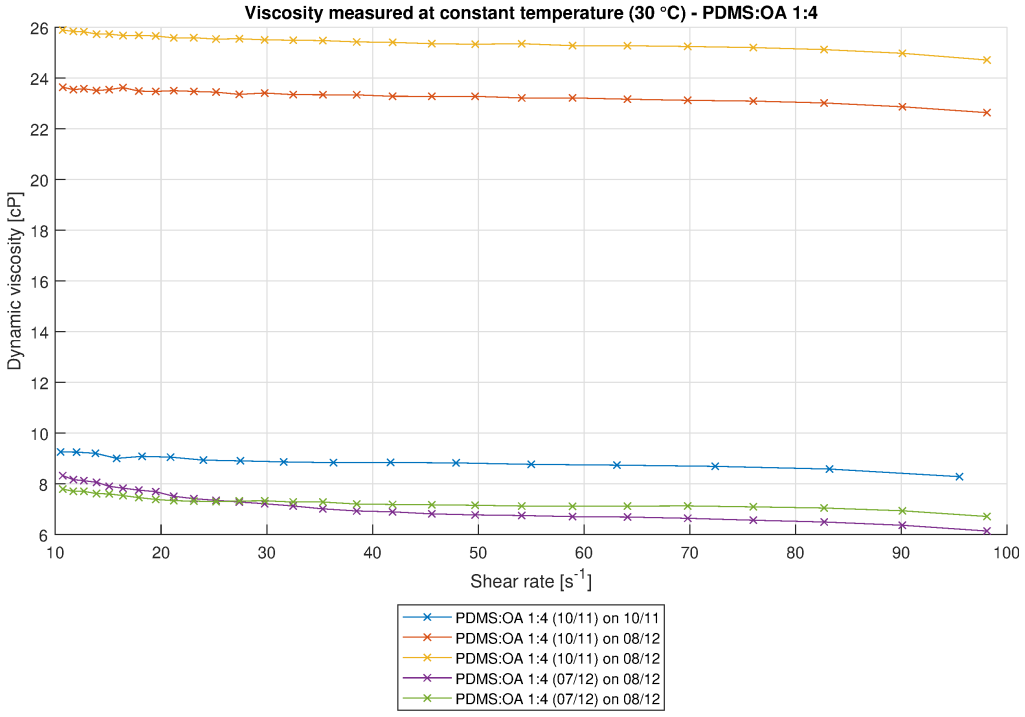

Figure 5.3: Viscosity measurements at a constant temperature of 30°C of PDMS:OA 1:4

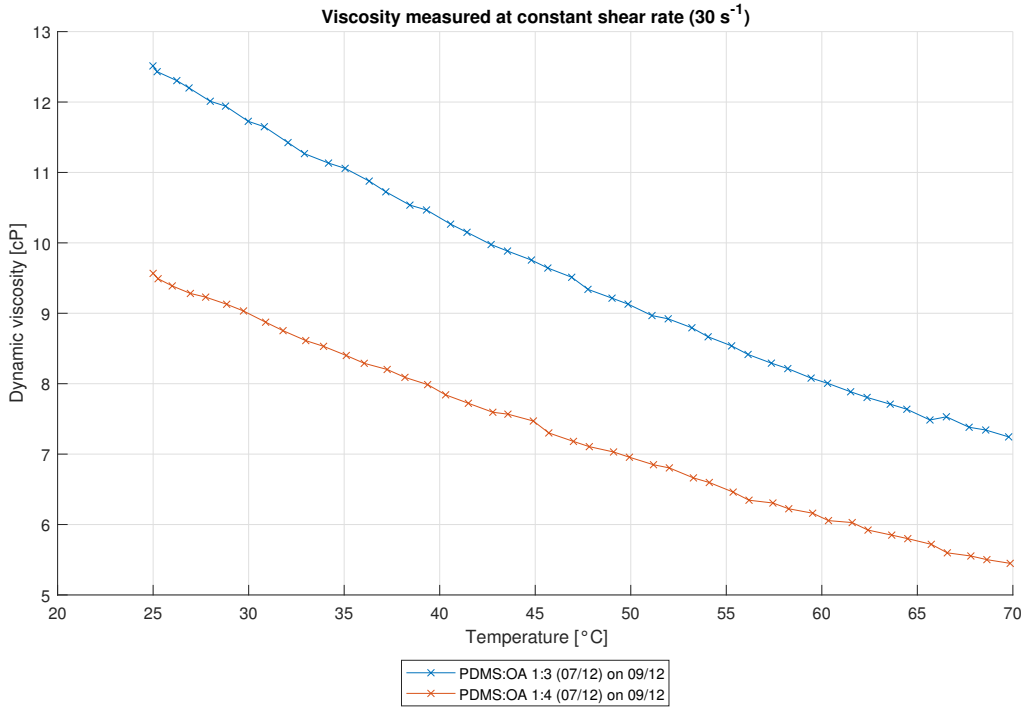

Figure 5.4: Viscosity of PDMS:OA 1:3 and 1:4 at a shear rate of $30s^{-1}$

Surface tension

The surface tension has been determined through a pendant drop test using the OCA 25 goniometer (DataPhysics Instruments). A surface tension higher than 40 mN/m can prevent the ink from properly jetting and a surface tension that is too low can result in satellite droplets. Both ratio formulations have been measured twice. A measurement consists of multiple runs where the goniometer automatically dispenses droplets and determines the surface tension for each drop, derived from its curvature at maximum volume. Figure 5.5 shows a droplet of PDMS:OA 1:4 at its maximum volume, right before it drops. As recommended by the machine supervisor, the runs with a measurement error of $\geq 0.4\mu$m are not taken into account when calculating the result of the measurement. The surface tension of PDMS:OA 1:3 is found to be 22.84 ± 0.18 mN/m ($n = 38$) and 23.86 ± 0.05 mN/m ($n = 28$) for PDMS:OA 1:4. See appendix D for plots of the data. During these tests, both ink formulations crept up the outside of the needle before reaching a certain droplet mass that was heavy enough to form a drop at the end of the needle.

Figure 5.5: Pendant drop test with PDMS:OA 1:4 ink, image captured at maximum volume

Particle size
The particle size of the ink components must be small enough to prevent clogging of the nozzle diameter. Lukic et al. advice a particle size of less than 10% of the nozzle diameter [36]. If the PDMS base and catalyst parts are stirred well during ink preparation, the PDMS will dissolve completely in the octyl acetate so the PDMS:OA ink will not contain any particles that can block the nozzle. However, the nozzle can still get clogged when the solvent evaporates causing the PDMS to solidify.

Z-value
Fromm proposed the Z-value as a dimensionless parameter to describe the behaviour of liquid drops [39]. This parameter relates the viscosity and surface tension through the dimensionless Ohnesorge number *Oh*, which is defined by the Reynolds number *Re* and Weber number *We*, all defined as shown in equation 5.1 through equation 5.4. A Z-value lower than 1 indicates an ink that is too viscous, and a Z-value higher than 10 results in the formation of multiple satellite droplets instead of a single droplet [38, 39].

$$Re = \frac{\rho u d}{\nu} \tag{5.1}$$

$$We = \frac{\rho u^2 d}{\gamma} \tag{5.2}$$

$$Oh = \frac{\sqrt{We}}{Re} \tag{5.3}$$

$$Z = Oh^{-1} = \frac{(d\rho\gamma)^{1/2}}{\nu} \tag{5.4}$$

Where:
ρ = density of the fluid
u = velocity
d = diameter of the nozzle aperture
ν = dynamic viscosity
γ = surface tension

Table 5.2: Characterised properties of PDMS:OA ink

PDMS:OA	**1:3**	**1:4**
Viscosity	14.552 cP	8.892 cP
Surface tension	22.84 ± 0.18 mN/m	23.86 ± 0.05 mN/m
Density	0.8398 ± 0.030 g/mL	0.8688 ± 0.0078 g/mL
Calculated Z-value	1.396	2.374

5.1.2. Ink stability
The ink remains liquid even after multiple days of storage in a glass bottle at room temperature, although this is dependent on the type of container used. To illustrate this, figure 5.6 shows a photo of two bottles taken on October 19th, where the bottle on the left is filled with 1:4 solution from October 10th and the smaller bottle on the right is filled with a 1:4 solution prepared on September 29th. The solvent has evaporated from the larger bottle causing the PDMS to cure and become gel-like, whereas the older PDMS:OA formulation in the small bottle appears to have lost no solvent at all and remains liquid. This makes the left bottle unfit for (long-term) PDMS:OA solutions storage.

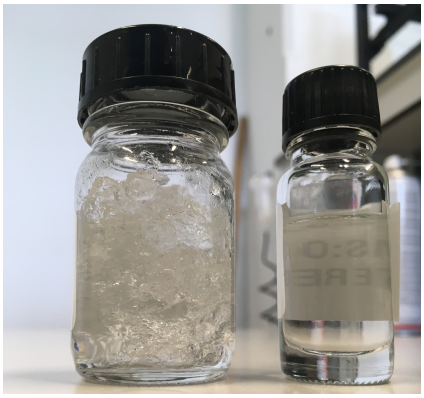

Figure 5.6: PDMS:OA 1:4 solutions stored in two different types of container, prepared on the 29th of September (right bottle) and on the 10th of October (left bottle). The left mixture has solidified, whereas the ink on the right is still fluid.

5.2. Printing

After formulating the PDMS:OA solutions, trial prints were performed to find the right settings for the printer. Many variables influence the print process, which are mostly optimised by trial-and-error. For more background on these settings, see section 2.1.

5.2.1. Settings

The PDMS:OA inks were rather difficult to print with. The 1:4 formulation is better jettable than the 1:3 formulation, which has difficulties with pinching off a droplet from the main tail. In general, a heated printhead at 30° C or higher was required to allow the ink to flow. The PDMS:OA inks performed better at low jetting frequencies, around 1500 Hz or in extreme cases even as low as 150 Hz.

5.2.2. Waveform

The first waveform used to produce droplets can be seen in figure 5.7a. This waveform is based on a standard waveform for Dimatix DMC-11610, as a starting point to fine tune the waveform for optimal droplet size and speed. In the DropAnalysis Results window in figure 5.7b several droplets are visible and a rogue-jetting nozzle at the left. This is probably caused by some excess fluid around the nozzle that diverts the trajectory of the jetted fluid.

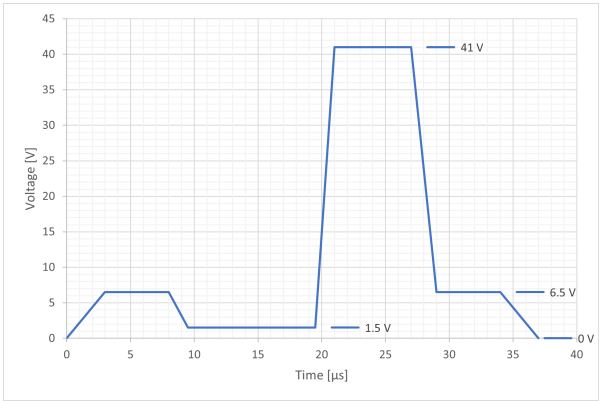

(a) Waveform used to produce drops in figure 5.7b

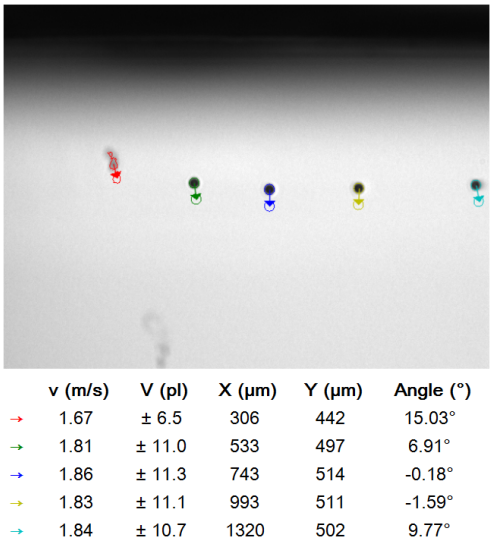

	v (m/s)	V (pl)	X (µm)	Y (µm)	Angle (°)
→	1.67	± 6.5	306	442	15.03°
→	1.81	± 11.0	533	497	6.91°
→	1.86	± 11.3	743	514	-0.18°
→	1.83	± 11.1	993	511	-1.59°
→	1.84	± 10.7	1320	502	9.77°

(b) Screenshot of the PixDro printer software, showing droplets from nozzle 5 to 9

Figure 5.7: PDMS:OA 1:4 waveform and droplets

5.2.3. DPI experiments

To investigate the effect of changing the dots-per-inch (DPI) on the print, matrices were printed on PVA coated glass at 100, 150, 175 and 200 DPI. Close-ups of the results are shown in figure 5.8. At a DPI of 100, the droplets have an average diameter of 70 μm. From these figures, it can be seen that at 175 and 200 DPI some droplets are close enough to coalesce and create a puddle. Whether this behaviour would improve when printed on top of the bottom electrode could not be investigated, as printer malfunctions caused a blockade for experimenting with PDMS ink. After repairs, the PDMS:OA ink remained troublesome when attempting to produce jettable droplets. Due to the obstacle this formed to the rest of the research it was decided to continue with a spin coated PDMS layer.

5.3. Spin coat application

To spin coat the PDMS layer onto the printed bottom electrode, no surface treatment is necessary. A PDMS mixture is prepared in a 10:1 base:catalyst ratio. The samples are fixed to a microscope glass and the contact pad of the bottom electrode is covered with removable scotch tape, to prevent the PDMS from obstructing access to the contact pad for actuation. The spin coat recipes as stated in table 5.3 were configured to produce

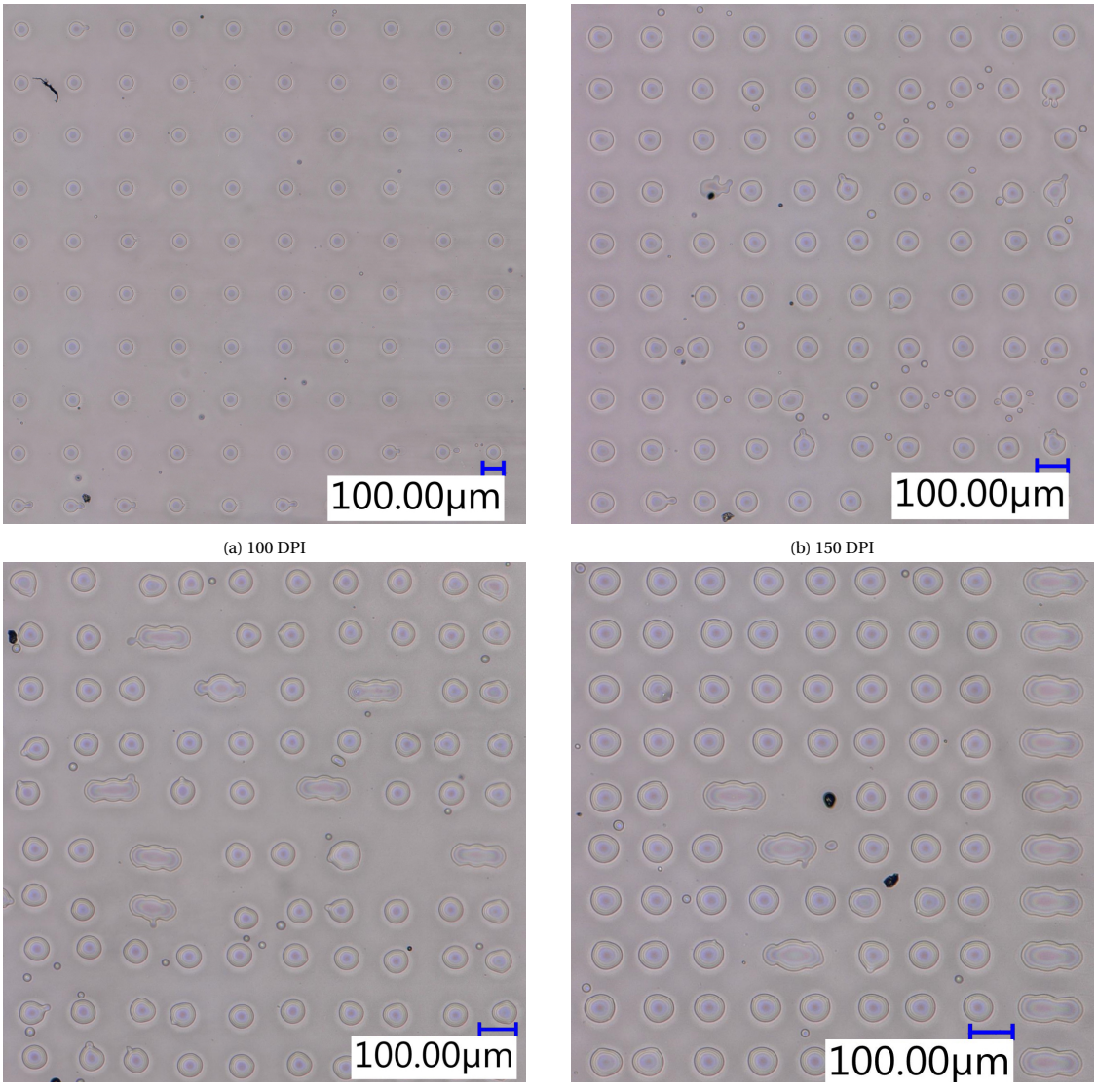

(a) 100 DPI

(b) 150 DPI

(c) 175 DPI

(d) 200 DPI

Figure 5.8: 10 by 10 px close-ups of printed PDMS at different DPI

a PDMS layer of approximately 10 μm, based on findings by Koschwanez et al.[40]. However, after measuring the thickness with a micrometer (accuracy ± 10 μm) it was determined that the resulting PDMS layer are significantly thicker than expected. Attempts at measuring the thickness using an interferometer for higher accuracy were unsuccessful due to the transparent nature of PDMS.

Table 5.3: Spin coat recipe settings

Speed	**Acceleration**	**Duration**	**Resulting thickness**
2000 RPM	500 RPM/s	300 s	approximately 30 μm
3000 RPM	500 RPM/s	300 s	approximately 25-30 μm

After application, the spin coated PDMS layer is cured on a hot plate for 60 minutes at 100 °C. The curing temperature and duration influence the stiffness of the PDMS [41, 42]. During this research, the curing settings have been chosen for relatively quick curing at a medium temperature, to limit the duration of the entire sample manufacturing process.

5.4. Discussion

The PDMS:OA 1:4 ink was slightly easier to print with than the 1:3 formulation. This is probably due to the PDMS:OA 1:3 ink pushing the limits of printability, although it lies within the boundaries set by literature. When printed with a higher DPI value, the printed droplets coalesce into larger puddles instead of forming a homogeneous surface. Further research into surface treatment of the substrate, tweaking the ink formulation or fine tuning the print settings can improve print results. However, in order to obtain insights into the full fabrication process, it would be recommended to focus on inkjet printing PDMS as a subject of a future research. To enable this research to proceed, spin coating has been chosen as an alternative manufacturing method. An important factor in this decision was a significant period of downtime due to a malfunction in the PiXDRO. When resuming printing experiments with PDMS:OA ink (new batches) after the repairs were carried out, creating jettable droplets proved more difficult than before the malfunctions. Whether this is a result of ink formulation or any residual malfunctions within the printer or printhead cannot be pinpointed with certainty.

6

Top electrode

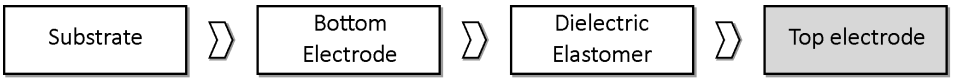

Figure 6.1: Location of the top electrode in the DEA structure

6.1. Materials

For the top electrode, both Mitsubishi NBSIJ-MU01 ink as well as Metalon JS-B25P (by NovaCentrix [43]) have been tested. These inks were both previously used in research in the Micro- and Nano Engineering department within TU Delft. For example, Bälz et al. [33] has printed P(VDF-TrFE-CTFE) actuators on the Novele substrate using an Epson home inkjet printer and carbon ink. In that research, the conductivity on Novele of both the Mitsubishi as well as the NovaCentrix ink have been examined. However, both AgNP inks have not been printed on top of the P(VDF-TrFE-CTFE) polymer layer. For the NovaCentrix ink, conducting results have been achieved by Bälz et al. by using an out-of-focus laser cutter as photonic curing method. Experiments with this method are required to test its viability as a post-processing method for an electrode printed on top of a polymer, which is part of the DEA central to this thesis.

6.2. Printing

After curing, the PDMS surface is too hydrophilic to allow directly printing on top. As a result, the printed silver droplets (Mitsubishi NBSIJ-01 ink) accumulate together into larger, separate droplets. Three different approaches have been explored to overcome this issue. The standard approach is to treat the PDMS surface with plasma, like oxygen or argon [44, 45]. Next to plasma treatment, in an effort to reduce the complexity of the manufacturing process, using a thin layer uncured PDMS as a medium for the printed silver has been tested. The third option, using a laser to reduce the surface energy, was only briefly considered as this had no effect on the transparent PDMS layer and caused significant damage to the electrode underneath. When printed on top of the PDMS layer, the self-sintering effect of the NBSIJ-MU01/Novele combination is lost. Thus, the NovaCentrix Metalon JS-B25P ink has been tested as well, although the jetting process is significantly less reliable than with the Mitsubishi ink. Figure 6.2 and 6.3 show the waveforms used with these inks.

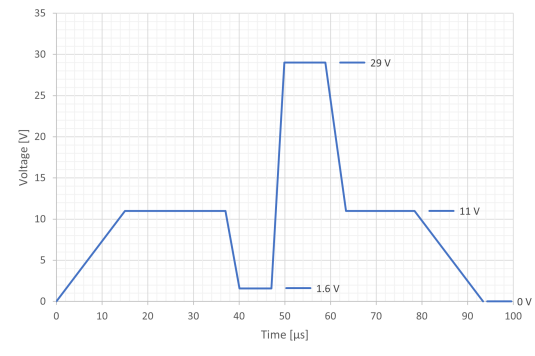

Figure 6.2: Base waveform for Mitsubishi NBSIJ-MU01

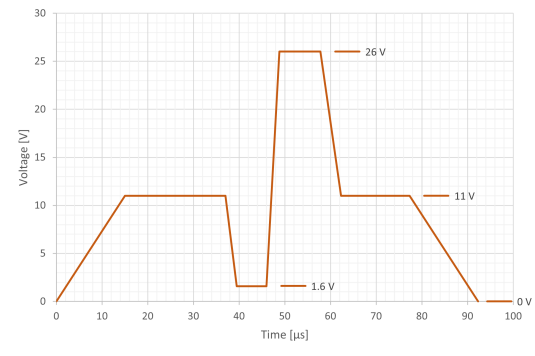

Figure 6.3: Base waveform for NovaCentrix Metalon JS-B25P

6.2.1. Uncured PDMS

One approach to create a more receptive surface to print the top electrode onto is based on the research by Sun et al. [46]. In this method, a thin layer of liquid PDMS is deposited on top of fully cured PDMS and the AgNP ink is printed into the liquid PDMS. The success of this method is greatly influenced by the heating time of the liquid PDMS layer. Figure 6.4 shows experiments with Mitsubishi NBSIJ-MU01 printed in completely uncured PDMS (on top of the fully cured PDMS layer). Multiple print passes were used to create a full coverage layer of silver. First, shown in figure 6.4a, one pass Y-bidirectional, then (figure 6.4b) one pass X-bidirectional and lastly two passes Y-bidirectional (figure 6.4c), all at 750 DPI. From these images, it is suspected that the liquid layer of PDMS is too thick and too liquid, leaving the silver droplets to "float" in the uncured PDMS. Figure 6.5a shows another print with the Mitsubishi AgNP ink in a semi-cured PDMS layer that has been heated at 100° C for 10 minutes. This appears to be too long already, as the ink creates a matrix of fused droplets. The resolution is better than when printed directly on top of fully cured PDMS, however, it is nowhere near 1000 DPI. This method has not been further explored, as it is still rather experimental compared to plasma cleaning. Nonetheless, this method could prove potentially interesting for a manufacturing process completely contained within the PiXDRO printer, if the PDMS layers can be printed as well. Otherwise, this method can still be used to reduce the total complexity of the manufacturing process when determining the right parameters for liquid PDMS layer thickness and level of curing.

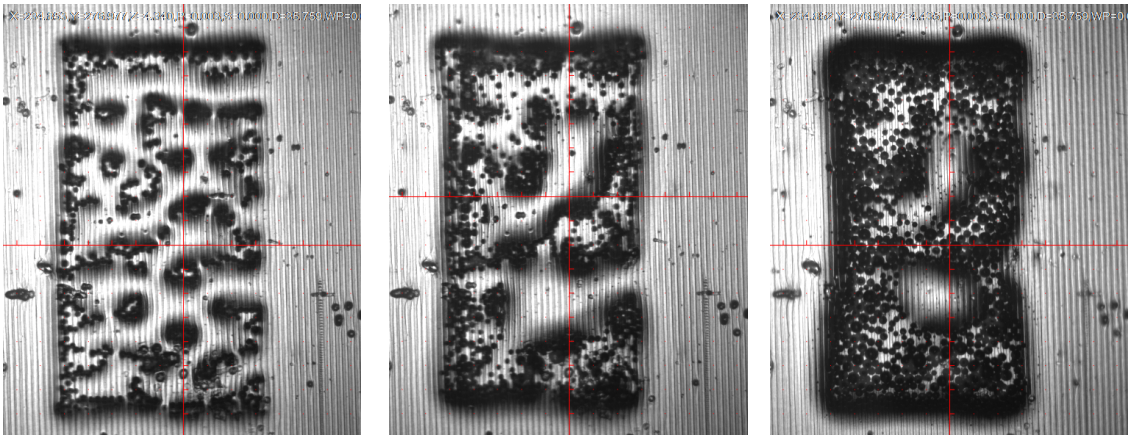

(a) First print: one pass Y-bidirectional (b) Second print: one pass X-bidirectional (c) Last print: two passes Y-bidirectional

Figure 6.4: Mitsubishi NBSIJ-01 on top of uncured PDMS, all prints at 750 DPI

6.2.2. Plasma treated PDMS

O_2 plasma activates the PDMS surface to increase the hydrophilicity. The plasma treatment is carried out in a plasma cleaner (Diener), exposing the sample to 80 W for 30 seconds. The difference between untreated and plasma treated PDMS can be seen in figure 6.5. Both figure 6.5a and figure 6.5b are prints of the same image, a rectangle of 30 by 50 px at a resolution of 1000 DPI. The difference is significant, which confirms the plasma treatment as the preferred surface treatment method.

A downside to this method is the time-dependency of the hydrophilic effect. Figure 6.6 shows a close-up of an electrode that has been printed five hours after the surface treatment. The separated drops of silver ink are an indication of the hydrophobic PDMS surface repairing itself. This behaviour appeared on multiple locations in the print. The signs of the PDMS repairing itself and recovering the hydrophobic surface has been observed in prints as early as around two hours after the plasma treatment, which limits the time available for printing the top electrode.

Mitsubishi NBSIJ-MU01

Prints with the NBSIJ-MU01 ink start cracking quickly. Figure 6.7 shows a drying print, directly after printing (figure 6.7a), when almost dry (figure 6.7b) and after four more minutes (figure 6.7c). Several tests with different print settings (for example changing print speed, bed temperature and print sizes) have been carried out, but cracking persisted around surface impurities and after heat treatment.

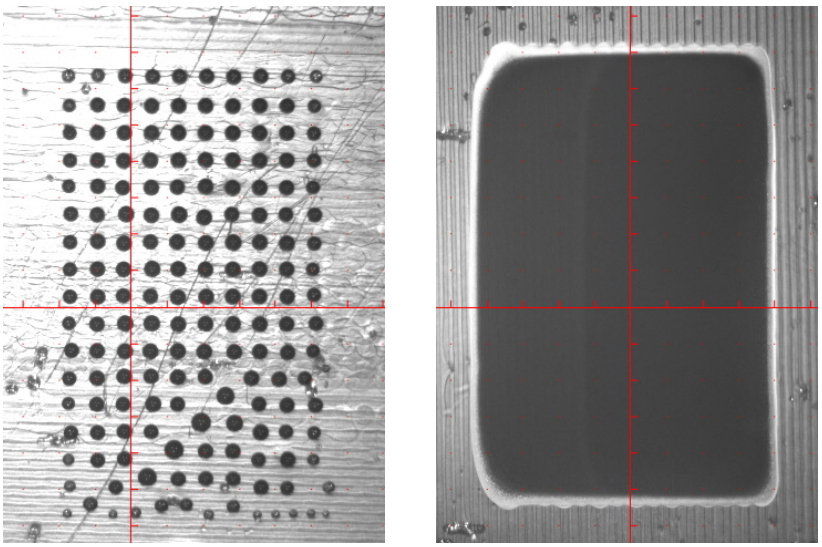

(a) Print on semi-cured PDMS (b) Print on plasma treated PDMS

Figure 6.5: Comparison of printing on top of uncured PDMS and plasma treated PDMS, both 30 by 50 px at 1000 DPI

Figure 6.6: Close-up of an electrode printed five hours after surface treatment

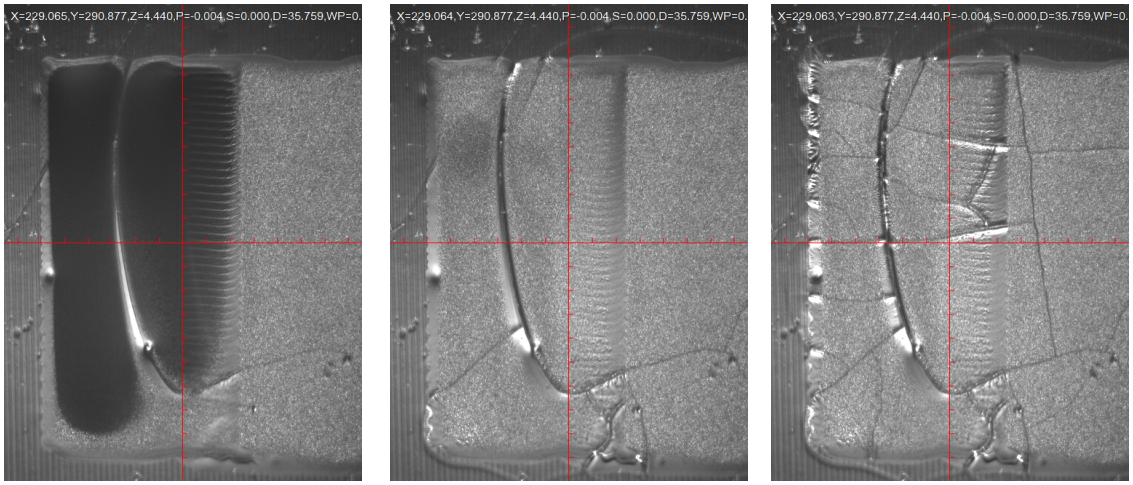

(a) Directly after printing (b) After 3 minutes and 8 seconds (c) After 7 minutes and 16 seconds

Figure 6.7: Mitsubishi NBSIJ-01 on top of plasma treated PDMS

Table 6.1: Results of thermal curing both AgNP inks at 250° C

		Conducting after curing at 250 °C			
Top electrode ink	**PDMS layer**	15 min	20 min	25 min	30 min
Mitsubishi NBSIJ-MU01	2000 RPM	No	No	No	No
	3000 RPM	No	No	No	No
NovaCentrix Metalon JS-B25P	2000 RPM	No	No	No	No
	3000 RPM	No	No	No	No

NovaCentrix Metalon JS-B25P
Due to the cracking of the Mitsubishi ink, prints were carried out with NovaCentrix Metalon JS-B25P ink as an alternative for the top electrode. This ink is harder to print with due to its tendency for clogging and unreliable jetting behaviour. In figure 6.8, it can be seen that the printed electrode does not show cracking, even around large print defects due to irregularities on the PDMS surface. A close-up can be seen in figure 6.9.

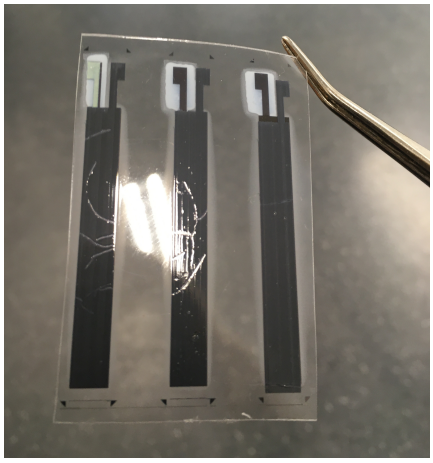

Figure 6.8: Photograph of top electrodes printed with NovaCentrix Metalon JS-B25P

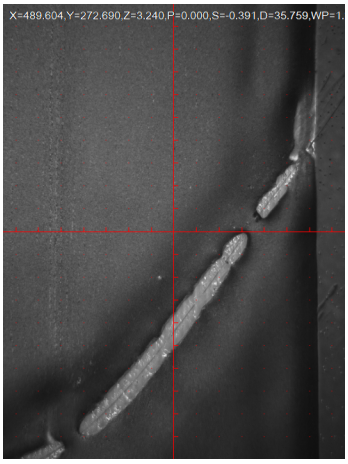

Figure 6.9: Close-up of a defect in the PDMS layer, electrode printed with JS-B25P ink

6.3. Post-processing

Finding a method to cure the silver ink on top of the PDMS layer proved challenging, as the Mitsubishi ink can no longer use the chemical sintering provided by the Novele substrate and the NovaCentrix ink required sintering methods that were not available during this research. Other methods of sintering the printed silver have been explored and the results will be discussed in this section.

6.3.1. Thermal sintering

According to NovaCentrix [47], the electrode printed with their AgNP ink should also be able to sinter when thermal cured at 250° C. Samples printed with the NovaCentrix and the Mitsubishi ink have been subjected to various temperatures for increasing durations on a hotplate. The samples consist of the Novele substrate with the bottom electrode (Mitsubishi NBSIJ-MU01 ink), two different PDMS thicknesses (spin coated at 2000 RPM and at 3000 RPM) and the top electrode. The results for the experiment at 250°C can be found in table 6.1, which shows that none of the samples were conducting.

6.3.2. Laser sintering

In previous research, Bälz et al. [33] has used an out-of-focus laser cutter (Optec) to photonically sinter silver electrodes printed on Novele substrates. This approach has been investigated as a method to sinter the top electrode of the DEA. The laser parameters from Bälz' paper were used as initial settings for experiments with a sample consisting of the Novele substrate with a bottom electrode (Mitsubishi NBSIJ-MU01), a cured PDMS layer and a top electrode printed with NovaCentrix Metalon JS-B25P ink. Small rectangular patches were targeted with the laser and optically inspected with the built-in camera before moving on to the next area with slightly adapted settings, such as laser power or number of repeats. An overview of the results of these experiments can be found in figure 6.11. Close-ups of the experiments can be found in appendix A.2.

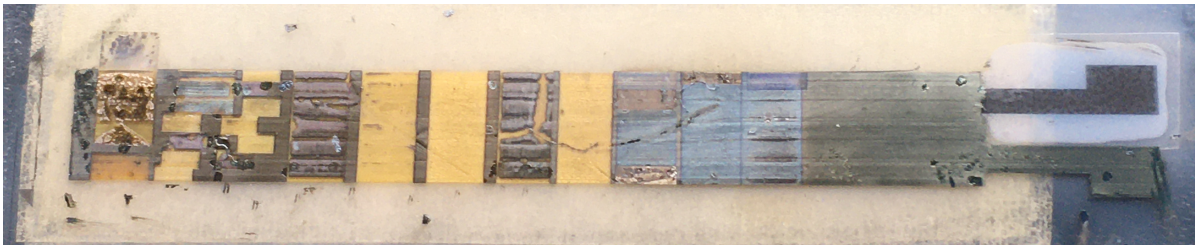

Figure 6.10: Photo of all laser sintering tests on top electrode

Despite all these attempts, none of the patches in figure A.2 and A.3 (in the appendix) were conducting after the laser treatment. Of all attempts shown in figure 6.11a only the patches outlined with the red boxes were conducting, but with a very high resistance. Figures 6.11b to 6.11d show close-ups of the three conducting patches, showing the flaky silver layers which are damaged at the locations the multimeter prong touched the silver.

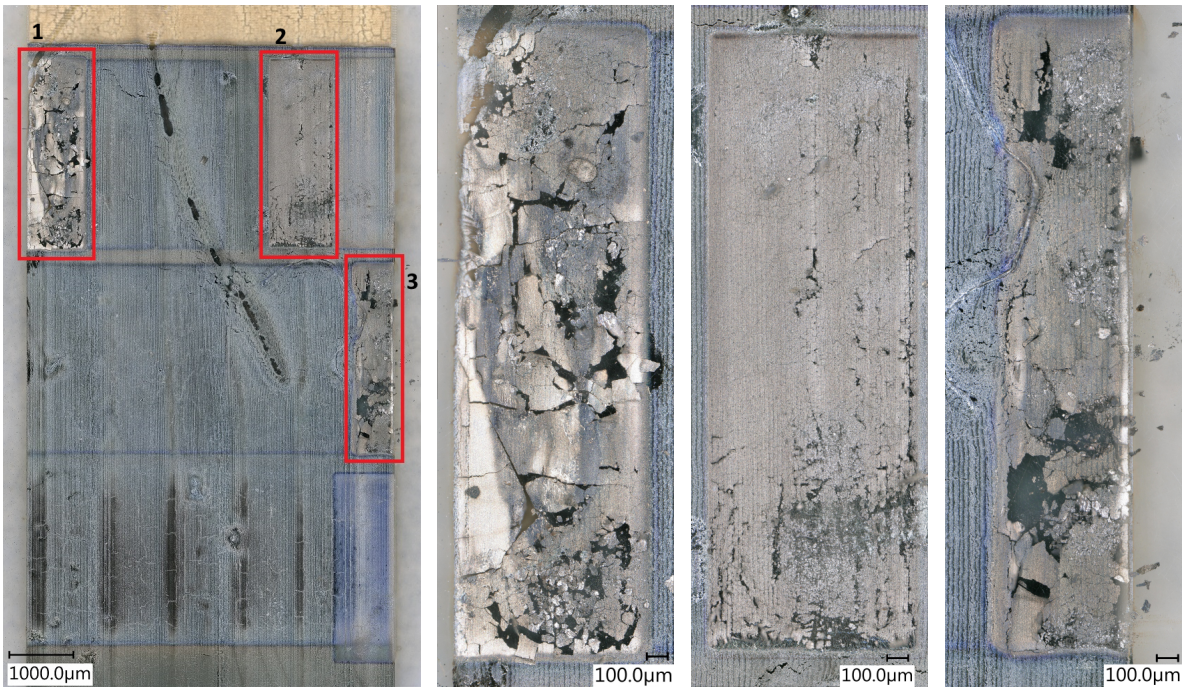

(a) Close-up of electrode area, conducting patches outlined in red

(b) First conducting patch

(c) Second conducting patch

(d) Third conducting patch

Figure 6.11: (a) section of laser sintering experiments, (b)-(d) close-ups of conducting patches

Due to the trial-and-error and time-consuming nature of these experiments, with very little successful results, this method of sintering the top electrode cannot be recommended in this manufacturing process and has not been further explored.

6.4. Discussion

Both AgNP inks proved unsuccessful for creating a conducting electrode on top of the spin coated PDMS. This was to be expected, as both their manufacturer recommended post-processing methods were unavailable. However, when solely focussing on their printing behaviour, neither ink can be recommended for future research. The Mitsubishi NBSIJ-MU01 ink has dependable jetting behaviour, but has a tendency of cracking while drying on top of the PDMS layer. These cracks were severely intensified during attempts at thermal sintering the ink. The NovaCentrix Metalon ink is very sensitive to any surface impurities, such as dust or PDMS irregularities. It requires a considerable effort to produce stable droplets and jetting remains unreliable when not printed immediately. Despite these downsides, it cracks less than the Mitsubishi AgNP ink when drying.

None of the investigated alternative sintering methods proved to be a serious contender for the manufacturing of a dielectric elastomer actuator. Using an out-of-focus laser for photonic sintering was a destructive trial-and-error process, without satisfactory results. Thermal curing caused the samples with Mitsubishi silver print to crack further while remaining non-conductive and had little effect on the samples with NovaCentrix silver ink. However, it does have a negative effect on the Novele substrate, which is not capable of handling the temperatures over 100° C and will harden, curl and burn when exposed to the high temperature required to sinter the NovaCentrix ink (in theory). This temperature (250° C) will also increase the stiffness of the underlying PDMS layer, which will decrease the actuation output of the DEA.

7

Finite element analysis

In order to validate future actuation results of an inkjet printed low actuation voltage dielectric elastomer actuator, a finite element analysis has been created using COMSOL Multiphysics® software [48]. This can be used in future research to check the influence of different materials or to design more complex DEA structures.

Because this thesis research produced no actuation results, the work done by Poulin et al. [1] has been used to validate the assumptions done in the constitutive equations governing the electromechanical behavior of the DEA. In that research, they created a low actuation voltage DEA using pad-printing and developed a numerical model for the stiffening impact of the electrodes.

7.1. Physics

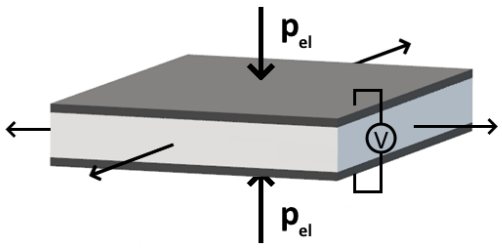

Figure 7.1: Schematic drawing of a DEA expanding under an applied voltage

The dielectric elastomer actuator is modelled as a parallel plate capacitor with a flexible elastomer as dielectric layer, as shown in figure 7.1. When applying a voltage between the electrodes, the opposite charges induce an electrostatic pressure (the Maxwell pressure) and squeeze the dielectric elastomer layer, which is approached in the model by applying a pressure on the elastomer as given in equation 7.1.

$$p_{el,ij} = \frac{1}{2}\epsilon_0\epsilon_r(E_i \cdot E_j - 0.5E^2) \tag{7.1}$$

The behaviour of the dielectric elastomer is approached by a hyperelastic material model. Several models exist, such as the Neo-Hookean [49], Gent [50], Boyce-Arruda [51], Ogden [52] and Yeoh [53] hyperelastic models. Choosing a suitable model depends on the expected strain and available material parameters [49]. For more information on the different hyperelastic material models, see appendix F [19]. Considering that this research did not yield any experimental data to fit the material parameters, the DEA is modelled as an incompressible Neo-Hookean material, as this model is based on a single material parameter (the shear modulus). All other materials in the model are modelled as linear elastic materials.

Electrostriction
In literature, some debate exists about the need for incorporating the effect of electrostriction into the modelling of dielectric elastomer actuators, however it is assumed to be negligible in PDMS due to its dielectric constant of 2.72 which is lower than the threshold of 4 identified by Lee et al. [54].

This assumption has been verified by incorporating the electrostrictive effect to the total stress response. According to the research by Shkel and Klingenberg [55–58], the electrostriction response of an isotropic material can be described by five material parameters:

- two Lamé parameters (λ [Pa] and μ [Pa])
- one dielectric constant (ϵ [-])
- two electrostriction parameters (α_1 [-] and α_2 [-])

The Lamé parameters and electrostriction parameters are given in equation 7.2 and 7.3, where Y is the Young's modulus [Pa], ν is the Poisson's ratio [-] and ϵ is the dielectric constant [-].

$$\lambda = \frac{Y\nu}{(1-2\nu)(1+\nu)} \qquad \mu = \frac{Y}{2(1+\nu)} \tag{7.2}$$

$$\alpha_1 = -\frac{2}{5}(\epsilon-1)^2 \qquad \alpha_2 = -\frac{1}{3}(\epsilon-1)(\epsilon+2)+\frac{2}{15}(\epsilon-1)^2 \tag{7.3}$$

The model has been compared to the measurements by Poulin et al., both with and without adding the electrostrictive effect to the constitutive equations. The measured and modelled results are plotted in figure 7.2. The modelled results in figure 7.2b, which take Maxwell pressure into account, show a good fit with the measurement results. However, when adding electrostriction to the constitutive equations as shown in figure 7.2c, it deviates from the trend in the measurement results.

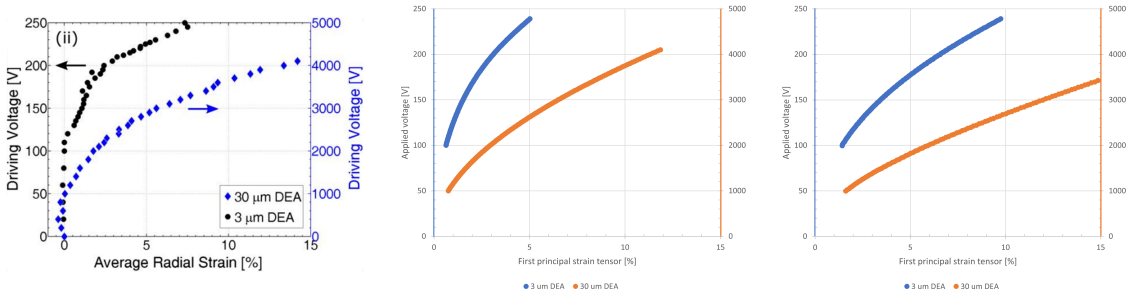

(a) Measurement results, taken from [1]

(b) Results with only Maxwell pressure

(c) Results with Maxwell pressure and electrostriction

Figure 7.2: Comparison of the models with measurements by Poulin et al. [1]

7.2. Model

Using the physics set up as described in section 7.1, it is possible to use the model to predict the behaviour of different geometries and DEA designs. The model is now set up as a very basic rectangular shape, but it is able to compute alternative designs, such as a cross shaped actuator and a partially actuated DEA (only covering a section of the dielectric elastomer with electrodes). The design aspect of the model fell outside of the scope of this research, as the experimental process was not capable of producing a working DEA to test such a design.

7.2.1. Parameters and variables

Table 7.1 lists all parameters defined for the model. The rectangular geometry of the DEA is controlled by the variables listed in tale 7.2, with the exception of `"V_applied"` which defines the electric field in the actuator.

7.2.2. Constraints

The boundaries of the substrate and elastomer and the edges of the shell are fixed at one of the short ends of the DEA, to simulate the clamp one would use in an actuation set-up and force the displacement into the other direction, creating a uni-directional cantilever. An added advantage is reducing computational errors. Errors due to dielectric breakdown are prevented by adding the parameter `"V_max"` to restrict the maximum voltage of a parametric sweep.

Due to the large aspect ratios in the geometry, the electrodes are modelled as a shell with thickness `"z_elec"` on both sides of the dielectric elastomer layer. A prescribed displacement is applied to couple the displacement of the shell with the elastomer layer.

Table 7.1: Parameters used in COMSOL model

Name	Expression	Value	Description
ini_val	eps	2.22E-16	Initial value to prevent errors
E_applied	V_applied/z_pdms	1E8 V/m	Applied electric field
E_total	sqrt(E_x^2 + E_y^2 + E_z^2)	1E8 V/m	Total electric field
E_x	ini_val [V/m]	2.2204E-16 V/m	Electric field, x direction
E_y	ini_val [V/m]	2.2204E-16 V/m	Electric field, y direction
E_z	-E_applied	-1E8 V/m	Electric field, z direction
V_max	100 * z_pdms [V/m] * 10^6	-	Maximum applied voltage
eps_0	epsilon0_const	8.8542E-12 F/m	Vacuum constant
eps_r	2.72	2.72	Relative permittivity of PDMS
epsilon	epsilon0_const*eps_r	2.4083E-11 F/m	Dielectric permittivity of PDMS

Table 7.2: Variables used in COMSOL model

Name	Type	Description
x_elec	Dimension	Depth of electrode
y_elec	Dimension	Width of electrode
z_elec	Dimension	Thickness of electrode
x_pdms	Dimension	Depth of PDMS layer
y_pdms	Dimension	Width of PDMS layer
z_pdms	Dimension	Thickness of PDMS layer
x_beam	Dimension	Depth of structural layer
y_beam	Dimension	Width of structural layer
z_beam	Dimension	Thickness of structural laye
V_applied	Voltage	Applied potential

7.2.3. Mesh

The mesh is an important factor in managing the calculation time. The total number of nodes is greatly reduced by modelling the thin electrodes as shell elements. As these shell elements are meshed in 2D, their thickness is considered negligible which allows for a larger minimum element size when meshing the remaining geometry. The mesh is defined as a mapped mesh on the bottom boundary of the elastomer layer. The maximum element size is defined at 150 μm, which controls the amount of nodes on the large surfaces of the model. This mesh is swept onto the remaining boundaries of the geometry using the quadrilateral face meshing method creating hexahedra elements.

7.3. Results

To create an understanding of the impact of changing a certain variable on the model, a sensitivity study has been performed using five variables, as stated in table 7.3. The length and width of the electrode and PDMS layers are defined by x_{beam} and y_{beam}, so they follow the shape of the structural layer as shown in figure 7.3. The output of the actuator is defined as the deflection [μm] of the free end of the DEA, similar to a single clamped cantilever. The full set of results can be found in appendix G.

Table 7.3: Values used in the FEA parameter study

Variable	Values			
V_{applied}	250 V	300 V	350 V	
x_{beam}	1 mm	5 mm	10 mm	
y_{beam}	0.5 mm	1 mm	5 mm	
z_{pdms}	5 μm	15 μm	30 μm	45 μm
z_{beam}	10 μm	20 μm	35 μm	50 μm

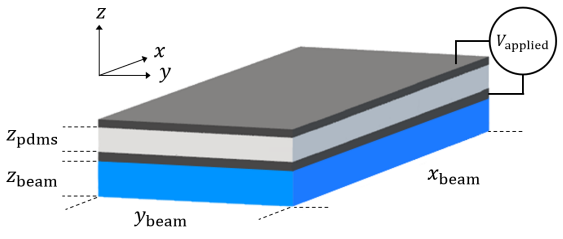

Figure 7.3: Schematic drawing indicating the variables of the DEA model

7.3.1. Analysis

To analyse these results, one specific set of variable values has been appointed as a benchmark value for each instance of V_{applied}, resulting in tables G.2, G.4 and G.6 containing the relative deflection [-]. This allows for quicker comparison between variable sets. The benchmark variable set and their corresponding deflection are listed below:

$V_{\text{applied}} = 250, 300, 350$ V

$x_{\text{beam}} = 5$ mm

$y_{\text{beam}} = 1$ mm

$z_{\text{pdms}} = 30$ μm

$z_{\text{beam}} = 35$ μm

250 V : deflection = 0.013291 μm

300 V : deflection = 0.019134 μm

350 V : deflection = 0.026037 μm

These values have been chosen as they represent a manufacturable DEA, where the PDMS layer is of a comparable thickness to the thickness achieved by spin coating in chapter 5 and the beam thickness is thinner than the Novele substrate (see also chapter 3) albeit still of substantial thickness. Three voltages have been chosen around 300 V to shown the influence of a relatively small change in applied voltage.

7.3.2. Impact of the variables on the output

When examining the results in appendix G, several patterns can be identified. Looking at each variable, the conclusions as summarized in table 7.4 describe the general influence they have on the output. While the output generally increases for larger y_{beam}, there are instances where the output very lightly decreases relative to the lower value. Despite this, the influence of y_{beam} on the output is almost negligible compared to the influence of the other variables.

Table 7.4: General conclusions on variable influence

Variable	Change in variable	Change in output
V_{applied}	Increases	Increases
x_{beam}	Increases	Increases
y_{beam}	Increases	Mostly increases
z_{pdms}	Increases	Decreases
z_{beam}	Increases	Decreases

The best output is found when z_{pdms} is at its smallest, but caution should be taken with applying the voltage to very thin dielectric layers due to the (electro)mechanical limits of the material. Nonetheless, the PDMS layer thickness proves to be the most important variable in the set. The least important variable is shown to be y_{beam}, especially when x_{beam} and z_{pdms} are smaller.

7.4. Discussion

During modelling it became clear that the mesh formed a crucial role in creating a computable model, due to the large aspect ratios in the very thin layers of the DEA. This has been addressed by modelling the electrodes as shell layers. While the experimental part of this thesis did not yield any actuation results on the manufactured DEA, this model can provide a theoretical basis for design choices in future research. Applicable as a basic model, the rectangular DEA shape can be expanded into more complex designs and the current materials can be easily exchanged for other materials, to explore their influence on the DEA performance. From the analysis run with the current model, it is shown that a thinner PDMS layer thickness is key to a higher actuator output.

8

Conclusion and recommendations

Finite element analysis of a low actuation voltage DEA
A minimal model has been built, producing fitting results with the research by Poulin et al. (2016). This is expected to correctly predict the influence of the design for similar low actuation voltage DEAs using PDMS as the dielectric elastomer. Unfortunately this can not be validated with original actuation results from the experimental part of this research as it has not produced a functional device. The model itself is able to handle different designs and is thus useful for future research projects involving the design of DEAs. Through a sensitivity study it is validated that reducing the PDMS layer thickness is vital for increasing the actuator output.

Inkjet-printing with the PiXDRO
In this research, insights into the techniques and sensitivities concerning the printing process for the PiXDRO were gained. Several printer limitations and settings require workarounds and fine-tuning to accommodate the research. It is highly recommended to be aware of these limitations (such as aborting the print when the temperature is out of bounds) and how they potentially impact the print, before starting a large print. The printer itself behaves rather erratic, which can be largely attributed to persisting faults in the Print Head Assembly (PHA) during the entire research.

Printing bottom electrode
Gained insights in how the Mitsubishi ink is influenced by printer settings. This ink shows very consistent jetting behaviour. Overall, this ink in combination with the Novele substrate can be recommended for future researches which do not require low stiffness. It is unclear whether this ink will show the same favourable behaviour on other substrates, however, its jetting behaviour remains a big advantage over the Novacentrix ink.

Creating dielectric elastomer layer with PDMS
Dilutions of PDMS and octyl acetate in 1:4 and 1:3 formulations have been produced, following research by Mikkonen et al. (2020). These formulations have been characterised on material parameters influencing the jetting behaviour. In theory, the 1:4 and 1:3 formulations should be able to print. In practice, both formulations are difficult to work with in the printer. It is unclear whether this is due to material effects (for example evaporation of the solvent or changes in viscosity) or due to the wrong printer settings or general malfunction of the PHA.

Spin coating non-diluted PDMS is an established method for creating PDMS membranes. The results are best when also desiccating after the PDMS mixture is poured onto the sample, prior to the spin cycle. The layer thicknesses produced with the spin cycles in this research are still quite thick for a low actuation voltage DEA, but it is possible to alter the spin cycle for thinner membranes. As actuation would not be possible before successfully creating the top electrode, no attempts at spinning a thinner layer have been made in the span of this research.

To prepare the cured PDMS layer, modifications to the surface are necessary due to its hydrophobicity. When treating the surface with O2-plasma for 30 seconds, the PDMS surface is printable for up to four hours, after which the quality of printing decreases. This method works well, however it is quite cumbersome as the total process takes up to 30 minutes in a clean room. Ideally, the substrate would never have to leave the printer during the manufacturing process.

Printing in semi-cured PDMS
This method could prove worthwhile for future research as it might benefit a higher actuation output of the DEA by creating more flexible electrodes. It can also reduce the risk of breakdown in air, as the electrode is directly encapsulated in an insulating layer.

Printing top electrode
Printing Mitsubishi ink on top of the plasma treated PDMS works well, however, the self-sintering nature of the ink does not work without the chemicals from the Novele substrate. It is not possible to sinter this ink by thermal curing. Novacentrix AgNP ink has been chosen as an alternative, which was not considered for the bottom ink as it is less consistent in its jetting behaviour. However, neither laser sintering nor heat curing was able to create a conducting electrode. This could have been foreseen as these curing methods are not specified by the manufacturer. Other types of conductive ink might behave favourable with the available curing methods, and should therefore be explored.

The result of the PDMS plasma treatment is imminent, but it decays over time, which creates a time pressure on printing the top electrode. This renders printing the top electrode with the Novacentrix ink even harder, as it requires a lot of time and effort to incite jetting and eventually reach sufficiently stable droplets to print with. This can not be prepared before the plasma cleaning, as that 30-minute process proves too long for the silver ink to remain stable and ready-to-jet.

Recommendations

Inkjet printing proves to be a serious contender for manufacturing low actuation voltage dielectric elastomer actuators. While it was not possible to complete a fully printed DEA sample, several steps can be taken to improve future results. To summarize:

Choose a thinner substrate or a sacrificial layer to lift the DEA, reducing the total stiffness
The thickness and stiffness of the rigid PET layer of the Novele substrate are an issue for creating a low actuation voltage DEA, as it will not be able to create enough force to produce significant actuation results.

Inkjet print with a different dielectric elastomer ink, preferably off-the-shelve
Other promising PDMS ink formulations from literature were not within reach during this research, but might prove to be a more reliable ink for printing.

Retry printing with PDMS:OA once the printer is fully repaired
The issues with the PDMS:OA ink were suspected to (partially) arise from the printer malfunctions. It was not an easy ink to print with before the malfunctions, but it worsened after the repairs.

Use a low temperature thermal curing or UV curing conducting ink for the electrodes
If the ink is curable at a low temperature it will not cause the PDMS to stiffen. If the ink is UV curable then it is possible to cure the printed electrode inside the PiXDRO printer.

Bibliography

[1] A. Poulin, S. Rosset, and H. Shea. Fully printed 3 microns thick dielectric elastomer actuator. In Yoseph Bar-Cohen and Frédéric Vidal, editors, *SPIE Smart Structures and Materials + Nondestructive Evaluation and Health Monitoring*, page 97980L, Las Vegas, Nevada, United States, April 2016.

[2] Jung-Hwan Youn, Seung Mo Jeong, Geonwoo Hwang, Hyunwoo Kim, Kyujin Hyeon, Jihwan Park, and Ki-Uk Kyung. Dielectric Elastomer Actuator for Soft Robotics Applications and Challenges. *Applied Sciences*, 10(2):640, January 2020.

[3] Roy Kornbluh. Chapter 8 - Fundamental configurations for dielectric elastomer actuators. In *Dielectric Elastomers as Electromechanical Transducers*, pages 79–90. Elsevier, 2008.

[4] Aaron P. Gerratt, Bavani Balakrisnan, Ivan Penskiy, and Sarah Bergbreiter. Dielectric elastomer actuators fabricated using a micro-molding process. *Smart Materials and Structures*, 23(5):055004, March 2014.

[5] G. Kofod, M. Paajanen, and S. Bauer. Self-organized minimum-energy structures for dielectric elastomer actuators. *Applied Physics A*, 85(2):141–143, November 2006.

[6] Yide Liu, Binhong Liu, Tenghao Yin, Yuhai Xiang, Haofei Zhou, and Shaoxing Qu. Bistable rotating mechanism based on dielectric elastomer actuator. *Smart Materials and Structures*, 29(1):015008, January 2020.

[7] Oluwaseun A. Araromi, Irina Gavrilovich, Jun Shintake, Samuel Rosset, Muriel Richard, Volker Gass, and Herbert R. Shea. Rollable Multisegment Dielectric Elastomer Minimum Energy Structures for a Deployable Microsatellite Gripper. *IEEE/ASME Transactions on Mechatronics*, 20(1):438–446, February 2015.

[8] Michele Ghilardi, Hugh Boys, Peter Török, James J. C. Busfield, and Federico Carpi. Smart Lenses with Electrically Tuneable Astigmatism. *Scientific Reports*, 9, November 2019.

[9] Ron Pelrine, Roy Kornbluh, and QB Pei. High-Speed Electrically Actuated Elastomers with Strain Greater Than 100%. *Science (New York, N.Y.)*, 287:836–9, March 2000.

[10] B. Tyler White and Timothy E. Long. Advances in Polymeric Materials for Electromechanical Devices. *Macromolecular Rapid Communications*, 40(1):1800521, 2019.

[11] Samuel Rosset and Herbert R. Shea. Flexible and stretchable electrodes for dielectric elastomer actuators. *Applied Physics A*, 110(2):281–307, February 2013.

[12] Benjamin O'Brien, Justin Thode, Iain Anderson, Emilio Calius, Enrico Haemmerle, and Shane Xie. Integrated extension sensor based on resistance and voltage measurement for a dielectric elastomer. In *Electroactive Polymer Actuators and Devices (EAPAD) 2007*, volume 6524, page 652415. International Society for Optics and Photonics, April 2007.

[13] Samuel Rosset, Oluwaseun A. Araromi, Samuel Schlatter, and Herbert R. Shea. Fabrication Process of Silicone-based Dielectric Elastomer Actuators. *Journal of Visualized Experiments*, (108):53423, February 2016.

[14] J. Oliveira, V. Correia, H. Castro, P. Martins, and S. Lanceros-Mendez. Polymer-based smart materials by printing technologies: Improving application and integration. *Additive Manufacturing*, 21:269–283, May 2018.

[15] David McCoul, Samuel Rosset, Samuel Schlatter, and Herbert Shea. Inkjet 3D printing of UV and thermal cure silicone elastomers for dielectric elastomer actuators. *Smart Materials and Structures*, 26(12):125022, December 2017.

[16] Riikka Mikkonen, Paula Puistola, Ilari Jönkkäri, and Matti Mäntysalo. Inkjet Printable Polydimethylsiloxane for All-Inkjet-Printed Multilayered Soft Electrical Applications. *ACS Applied Materials & Interfaces*, 12(10):11990–11997, March 2020.

[17] Samuel Schlatter, Giulio Grasso, Samuel Rosset, and Herbert Shea. Inkjet Printing of Complex Soft Machines with Densely Integrated Electrostatic Actuators. page 18, 2020.

[18] Alexandre Poulin, Samuel Rosset, and Herbert R. Shea. Printing low-voltage dielectric elastomer actuators. *Applied Physics Letters*, 107(24):244104, December 2015.

[19] Sanne Elschot. Inkjet-printing of dielectric elastomer actuators for bistable and bidirectional actuation. Literature review, July 2020.

[20] Liesbeth Mombers. Training PiXDRO LP50.

[21] Cornell. Ink Tutorial. https://www.cnfusers.cornell.edu/sites/default/files/Equipment-Resources/Ink%20formulation%20tutorial.pdf.

[22] Yuanyuan Liu and Brian Derby. Experimental study of the parameters for stable drop-on-demand inkjet performance. *Physics of Fluids*, 31(3):032004, March 2019.

[23] Muhammad Ali Shah, Duck-Gyu Lee, Bo Yeon Lee, Nam Woon Kim, Hyojin An, and Shin Hur. Actuating Voltage Waveform Optimization of Piezoelectric Inkjet Printhead for Suppression of Residual Vibrations. *Micromachines*, 11(10):900, September 2020.

[24] DMP 2800 User's Guide V2.0.

[25] NovaCentrix. Technical Data Sheet - Novele IJ-220 (Printed Electronics Substrate), May 2011.

[26] Kweku A. Addae-Mensah, Ronald S. Reiserer, and John P. Wikswo. Poly(vinyl alcohol) as a structure release layer for the microfabrication of polymer composite structures. *Journal of Micromechanics and Microengineering*, 17(7):N41–N46, May 2007.

[27] Mitsubishi Paper Mills Limited. Safety Data Sheet - NBSIJ-MU01 (Silver Nano Particle Ink), January 2014.

[28] Mitsubishi Paper Mills Limited. Silver Nano FAQ (Frequently Asked Questions) | Mitsubishi Paper Mills. https://www.mpm.co.jp/electronic/eng/silver-nano/faq.html, 2016.

[29] R. Verplancke, F. Bossuyt, D. Cuypers, and J. Vanfleteren. Thin-film stretchable electronics technology based on meandering interconnections: Fabrication and mechanical performance. *Journal of Micromechanics and Microengineering*, 22(1):015002, December 2011.

[30] Mario Gonzalez, Fabrice Axisa, Mathieu Vanden Bulcke, Dominique Brosteaux, Bart Vandevelde, and Jan Vanfleteren. Design of metal interconnects for stretchable electronic circuits. *Microelectronics Reliability*, 48(6):825–832, June 2008.

[31] Mohammed Benslimane, Peter Gravesen, and Peter Sommer-Larsen. Mechanical properties of dielectric elastomer actuators with smart metallic compliant electrodes. In *Smart Structures and Materials 2002: Electroactive Polymer Actuators and Devices (EAPAD)*, volume 4695, pages 150–157. International Society for Optics and Photonics, July 2002.

[32] Ned Bowden, Scott Brittain, Anthony G. Evans, John W. Hutchinson, and George M. Whitesides. Spontaneous formation of ordered structures in thin films of metals supported on an elastomeric polymer. *Nature*, 393(6681):146–149, May 1998.

[33] K. Keith Baelz and Andres Hunt. P(VDF-TrFE-CTFE) Actuators with Inkjet Printed Electrodes, November 2019.

[34] Dow Benelux BV. Safety Data Sheet - Sylgard 184 (Silicone Elastomer), October 2019.

[35] Sigma-Aldrich. Safety Data Sheet - Octyl Acetate (Solvent), April 2019.

[36] Maria Lukić, Jane Clarke, Christopher Tuck, William Whittow, and Garry Wells. Printability of elastomer latex for additive manufacturing or 3D printing. *Journal of Applied Polymer Science*, 133(4):n/a–n/a, January 2016.

[37] Alexander Kamyshny and Shlomo Magdassi. Inkjet Ink Formulations. In *Inkjet-Based Micromanufacturing*, chapter 12, pages 173–189. John Wiley & Sons, Ltd, 2012.

[38] Nilza Reis, Chris Ainsley, and Brian Derby. Ink-Jet Delivery of Particle Suspensions by Piezoelectric Droplet Ejectors. *Journal of Applied Physics*, 97, May 2005.

[39] J. E. Fromm. Numerical Calculation of the Fluid Dynamics of Drop-on-Demand Jets. *IBM Journal of Research and Development*, 28(3):322–333, May 1984.

[40] John H. Koschwanez, Robert H. Carlson, and Deirdre R. Meldrum. Thin PDMS Films Using Long Spin Times or Tert-Butyl Alcohol as a Solvent. *PLOS ONE*, 4(2):e4572, February 2009.

[41] F. Schneider, T. Fellner, J. Wilde, and U. Wallrabe. Mechanical properties of silicones for MEMS. *Journal of Micromechanics and Microengineering*, 18(6):065008, April 2008.

[42] I. D. Johnston, D. K. McCluskey, C. K. L. Tan, and M. C. Tracey. Mechanical characterization of bulk Sylgard 184 for microfluidics and microengineering. *Journal of Micromechanics and Microengineering*, 24(3):035017, February 2014.

[43] NovaCentrix. Technical Data Sheet - Metalon JS-B25P (Silver Inkjet Ink), March 2016.

[44] Samu Hemmilä, Juan V. Cauich-Rodríguez, Joose Kreutzer, and Pasi Kallio. Rapid, simple, and cost-effective treatments to achieve long-term hydrophilic PDMS surfaces. *Applied Surface Science*, 258(24):9864–9875, October 2012.

[45] Jumana M. Abu-Khalaf, Loiy Al-Ghussain, and Ala'aldeen Al-Halhouli. Fabrication of Stretchable Circuits on Polydimethylsiloxane (PDMS) Pre-Stretched Substrates by Inkjet Printing Silver Nanoparticles. *Materials*, 11(12):2377, December 2018.

[46] Jiazhen Sun, Jieke Jiang, Bin Bao, Si Wang, Min He, Xingye Zhang, and Yanlin Song. Fabrication of Bendable Circuits on a Polydimethylsiloxane (PDMS) Surface by Inkjet Printing Semi-Wrapped Structures. *Materials (Basel, Switzerland)*, 9(4), March 2016.

[47] NovaCentrix. Conductive Inks FAQ. https://www.novacentrix.com/conductive-inks-FAQ, July 2017.

[48] COMSOL Multiphysics®. COMSOL AB.

[49] NianFeng Wang, ChaoYu Cui, Hao Guo, BiCheng Chen, and XianMin Zhang. Advances in dielectric elastomer actuation technology. *Science China Technological Sciences*, 61(10):1512–1527, October 2018.

[50] A. N. Gent. A New Constitutive Relation for Rubber. *Rubber Chemistry and Technology*, 69(1):59–61, March 1996.

[51] Mary C. Boyce and Ellen M. Arruda. Constitutive Models of Rubber Elasticity: A Review. *Rubber Chemistry and Technology*, 73(3):504–523, July 2000.

[52] Raymond William Ogden and Rodney Hill. Large deformation isotropic elasticity – on the correlation of theory and experiment for incompressible rubberlike solids. *Proceedings of the Royal Society of London. A. Mathematical and Physical Sciences*, 326(1567):565–584, February 1972.

[53] O. H. Yeoh. Some Forms of the Strain Energy Function for Rubber. *Rubber Chemistry and Technology*, 66(5):754–771, November 1993.

[54] Ho Lee, Yiyan Peng, and Yuri Shkel. Strain-dielectric response of dielectrics as foundation for electrostriction stresses. *Journal of Applied Physics*, 98, October 2005.

[55] Yuri Shkel. Electrostriction: Material parameters and stress/strain constitutive relations. *Philosophical Magazine*, 87:1743–1767, April 2007.

[56] Yuri Shkel and Daniel Klingenberg. Dielectric Parameters for Electrostriction of Solids. March 1997.

[57] Yuri Shkel and Daniel Klingenberg. Material parameters for electrostriction. *Journal of Applied Physics*, 80:4566–4572, November 1996.

[58] Yuri M. Shkel and Daniel J. Klingenberg. Electrostriction of polarizable materials: Comparison of models with experimental data. *Journal of Applied Physics*, 83(12):7834–7843, May 1998.

[59] Zhigang Suo. Theory of dielectric elastomers. *Acta Mechanica Solida Sinica*, 23(6):549–578, December 2010.

[60] Ying Shi Teh and Soo Jin Adrian Koh. Giant continuously-tunable actuation of a dielectric elastomer ring actuator. *Extreme Mechanics Letters*, 9:195–203, December 2016.

[61] NovaCentrix. Safety Data Sheet - Metalon JS-B25P (Silver Inkjet Ink), September 2016.

A

Addition images

A.1. Print directions

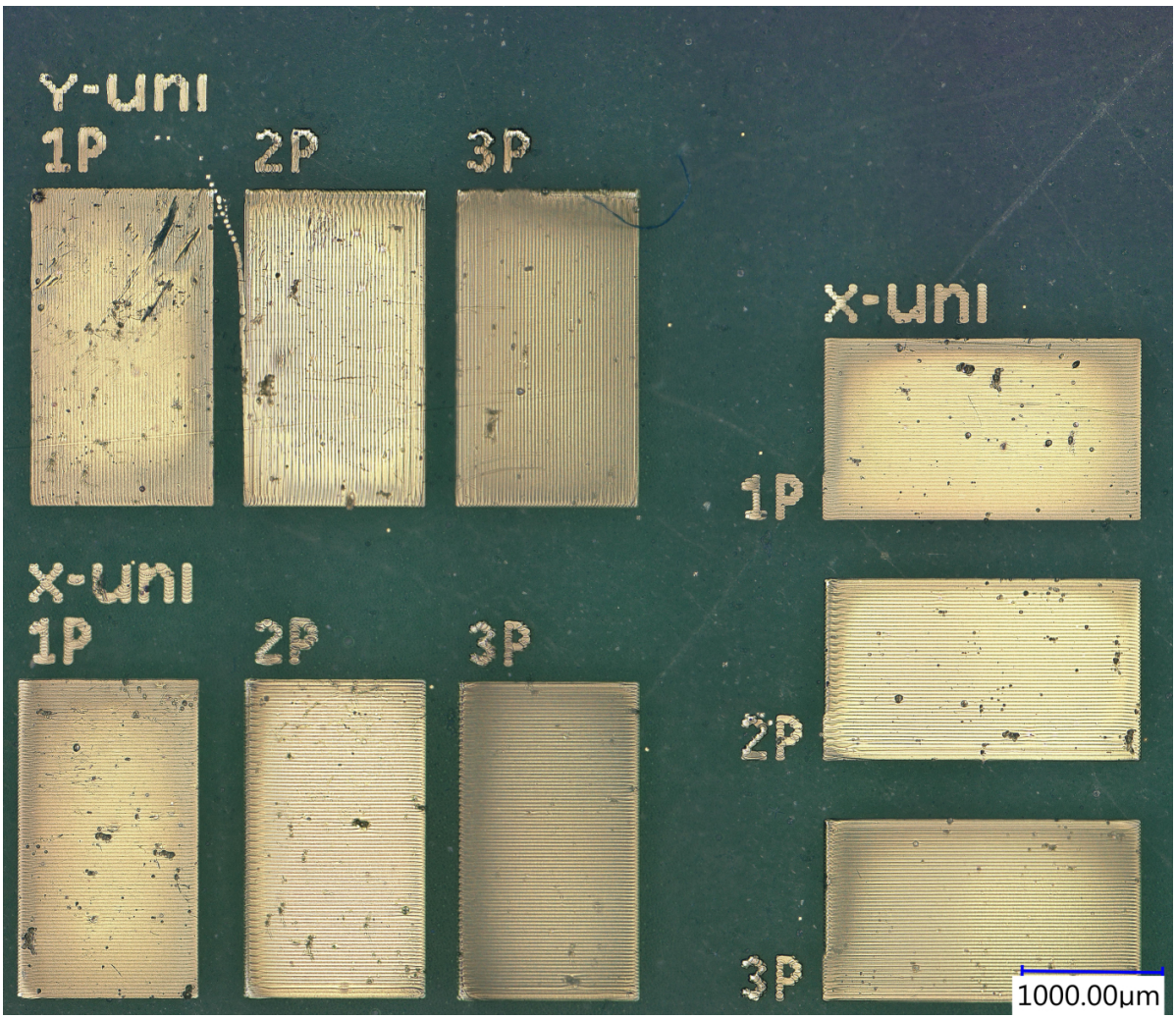

Figure A.1: Mitsubishi NBSIJ-01 printed on top of Novele IJ-220. Overview of prints with different print directions

A.2. Results of top electrode laser sintering tests

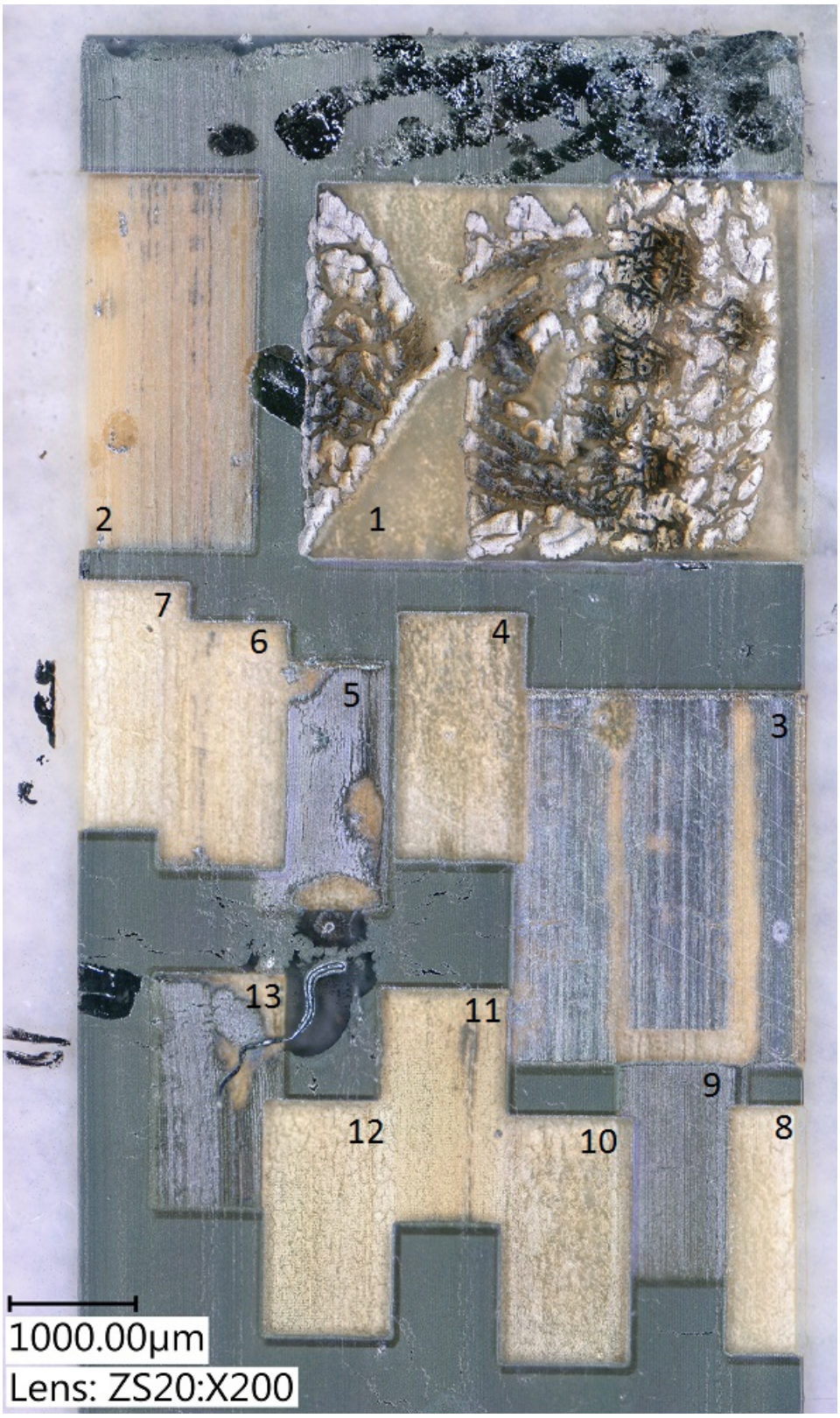

Figure A.2: Small patches #1 to #13

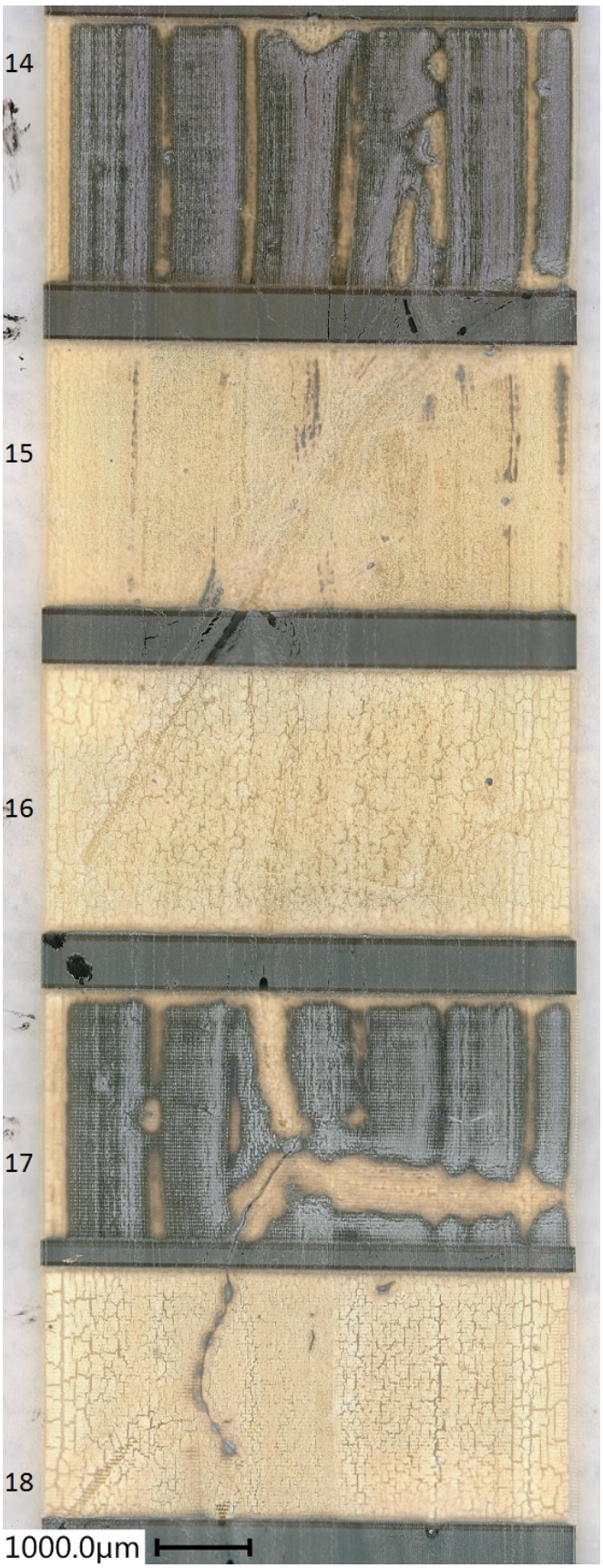

Figure A.3: Large patches #14 to #18

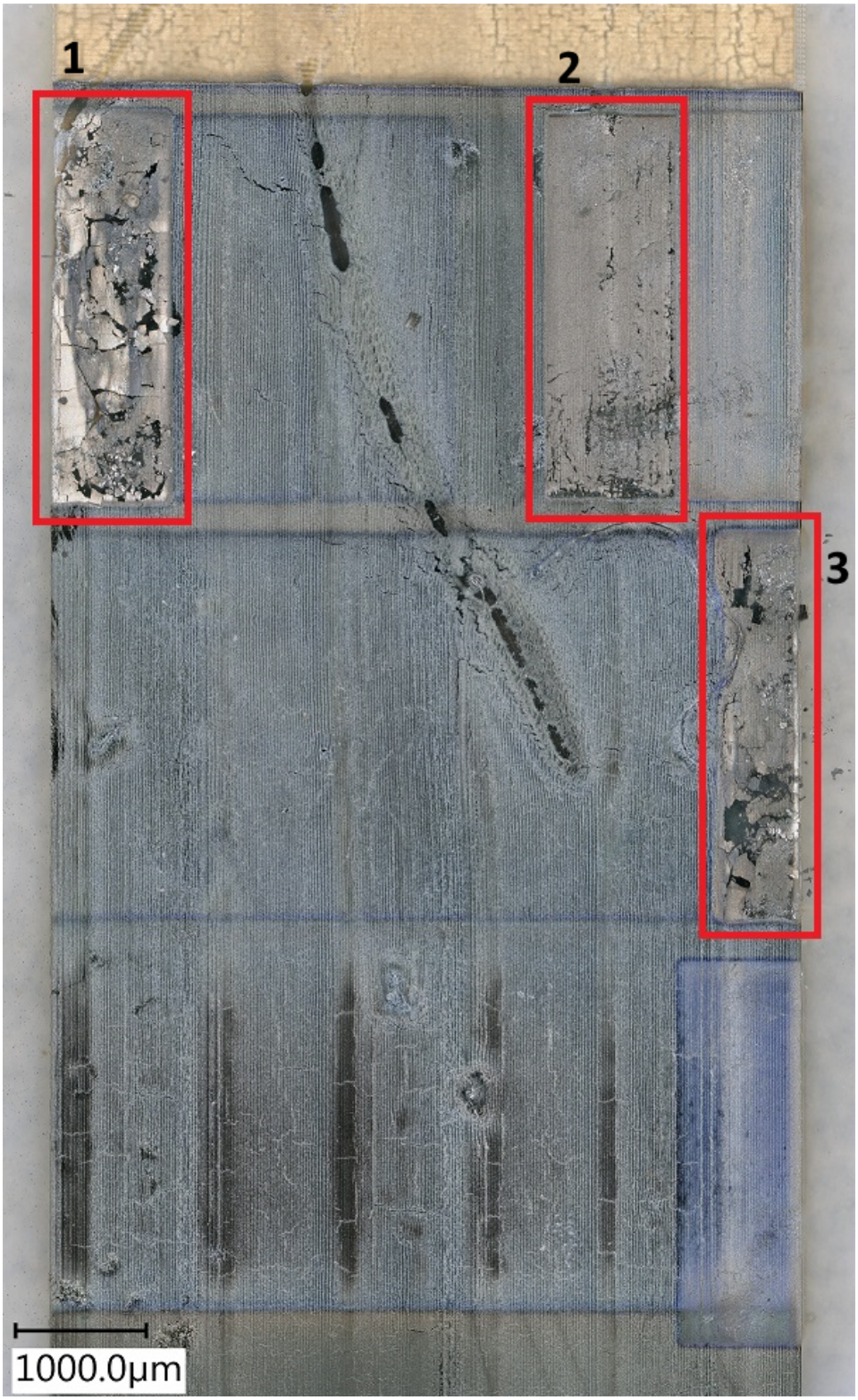

Figure A.4: Results of second laser sintering attempt. Red boxes indicating conducting patches

B

Interferometer measurements

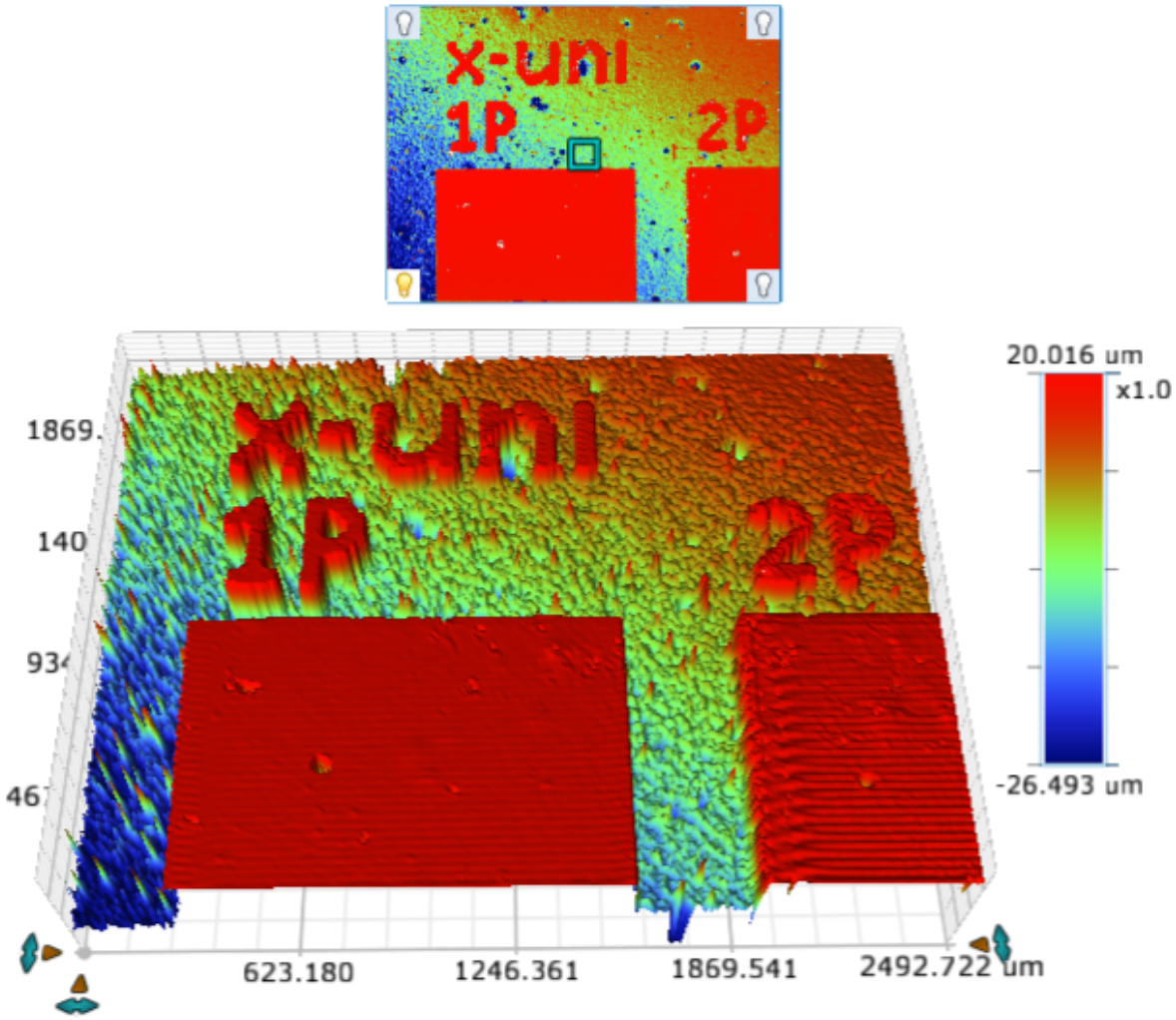

Figure B.1: Mitsubishi NBSIJ-01 printed on top of Novele IJ-220

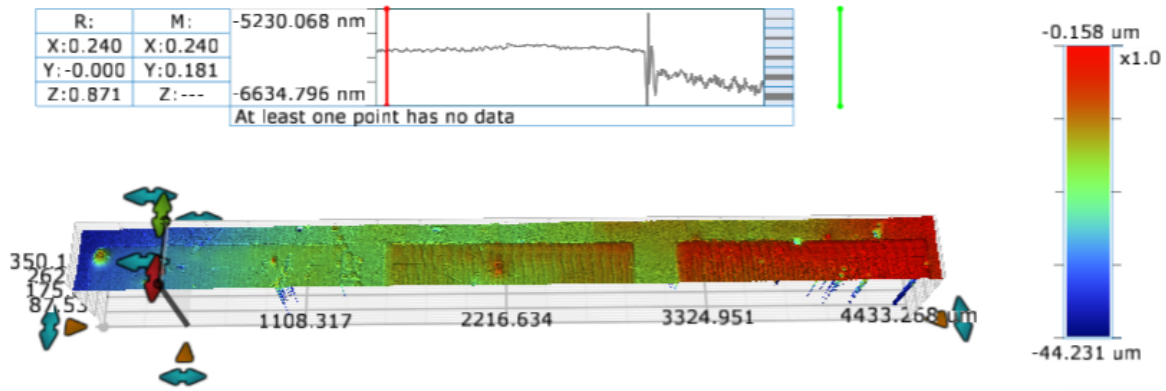

(a) Y-unidirectional print - 1 pass

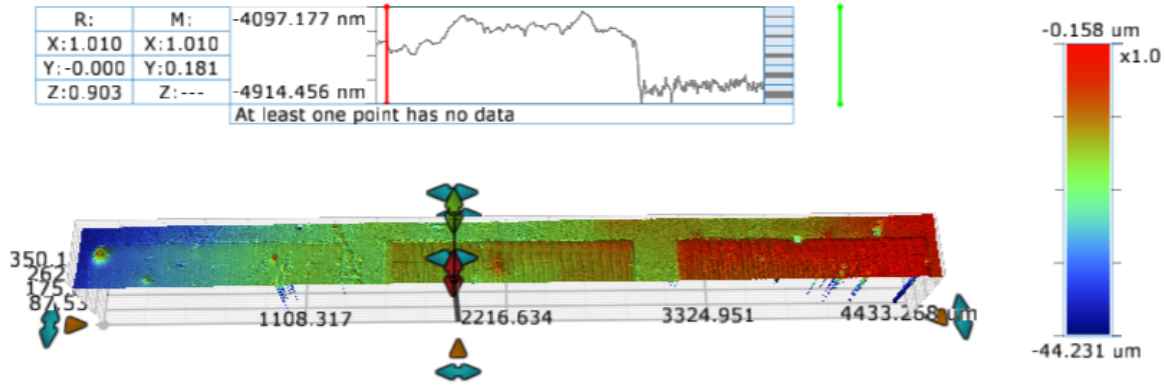

(b) Y-unidirectional print - 2 passes

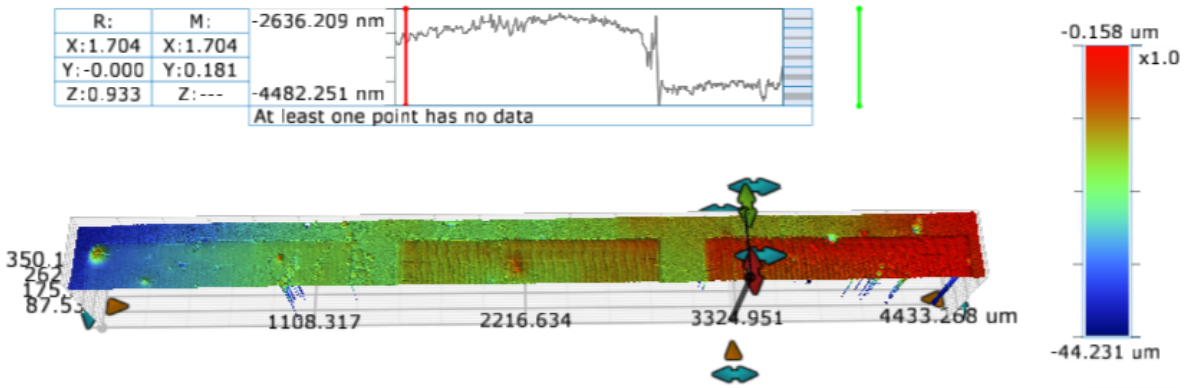

(c) Y-unidirectional print - 3 passes

Figure B.2: Thickness measurements of multiple passes with Mitsubishi NBSIJ-01 on Novele IJ-220

C

Tape tests

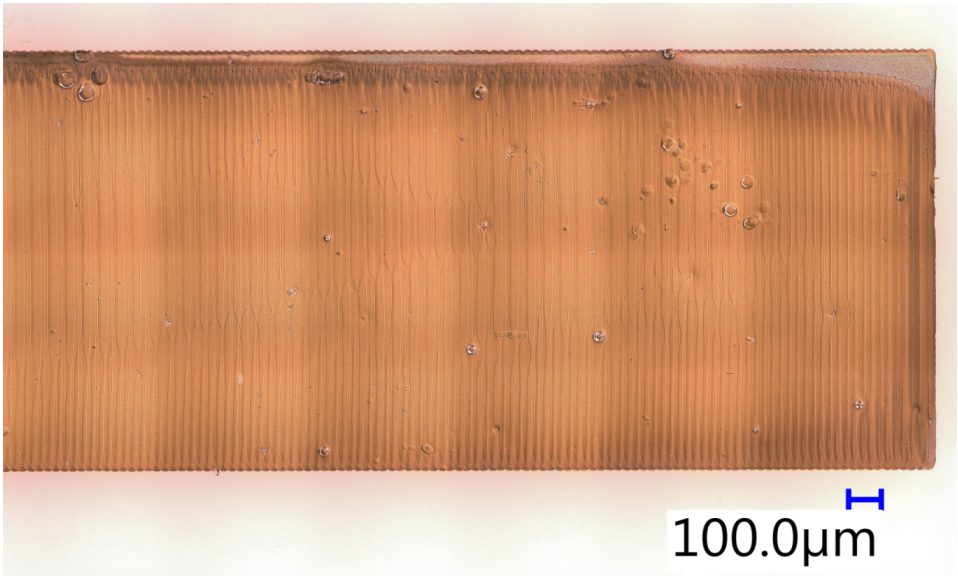

Figure C.1: Close-up of electrode before applying tape

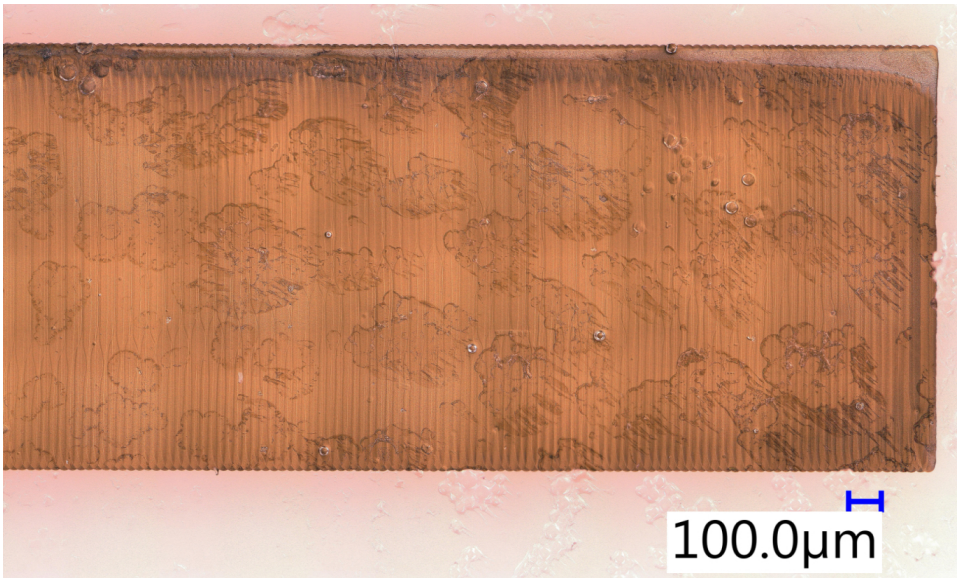

Figure C.2: Close-up of electrode after removing tape, with glue residue

D

PDMS:OA ink characterisation

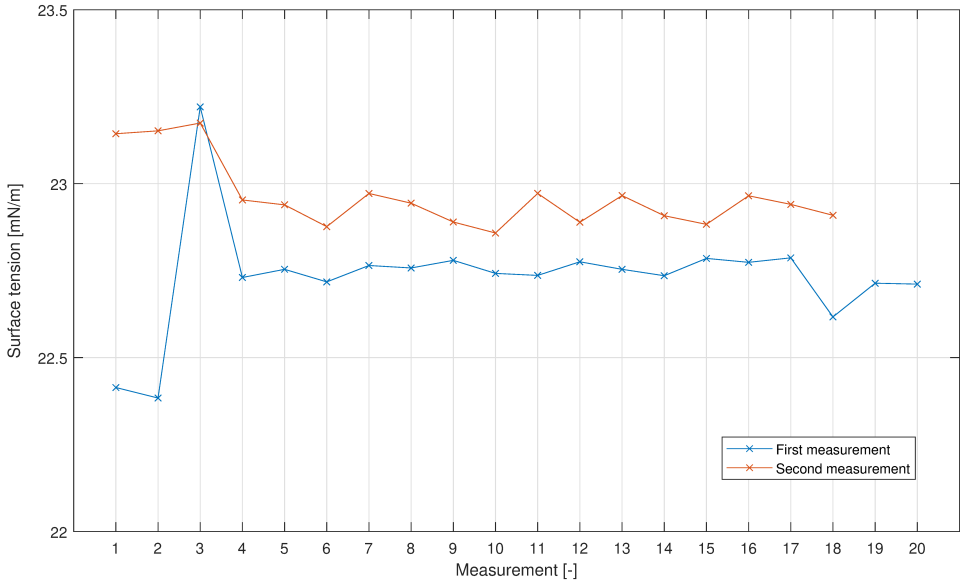

Figure D.1: Surface tension measurements of PDMS:OA 1:3

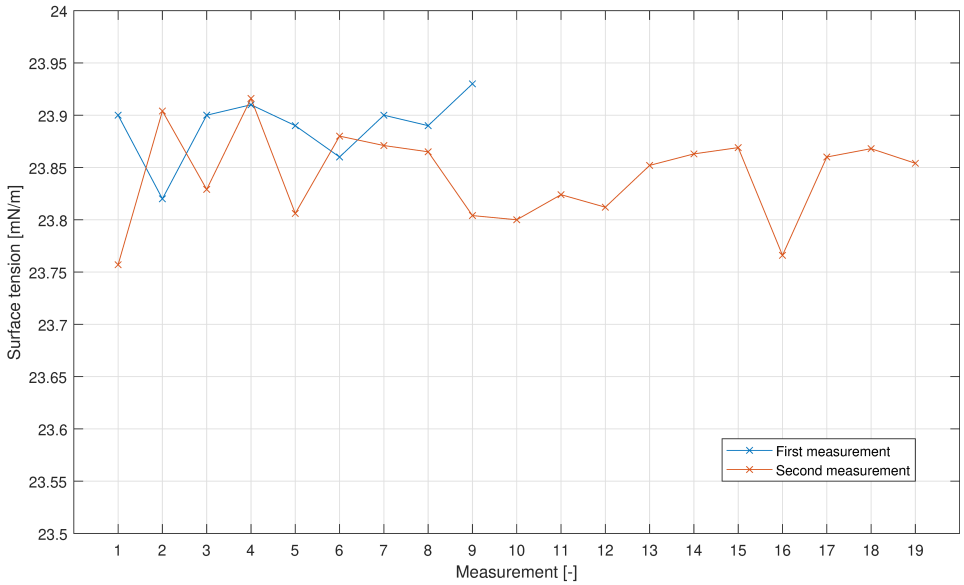

Figure D.2: Surface tension measurements of PDMS:OA 1:4

E

Equipment used

Characterisation

- Viscosity measurement: Rheometer MCR 302 (Anton Paar)
- Surface tension: OCA 25 (DataPhysics Instruments)
- Density: Laboratory scale
- Metrology: White light interferometer K1 (Bruker)
- Microscope: Digital Microscope VHX-6000 (Keyence)

Fabrication

- Inkjet printer: PiXDRO LP50 V5.0 (Süss-MicroTec)
- PHA: DMC printhead - 10 pL (FUJIFILM Dimatix)
- Spincoater: SPIN150i (Polos)
- Plasma cleaner: Femto (Diemer)
- Laser: Micro laser etching machine (Optec)

Materials

- Substrate: Novele IJ-220 (NovaCentrix [25])
- AgNP ink: NBSIJ-MU01 (Mitsubishi) [27]
- AgNP ink: Metalon JS-B25P (Novacentrix) [61]
- Dielectric elastomer: Sylgard-184 (Dow Corning) [34]
- Solvent (for PDMS ink): Octyl-acetate (Sigma-Aldrich) [35]

F

Hyperelastic material models

Dielectric elastomer actuators are capable of much larger strains than 10%, so complex models are required to approach the electromechanical behaviour realistically. Wang et al. summarized the most frequently used hyperelastic models in table F.1, where type A refers to micromechanical models, which considers the underlying structure of the material, type B refers to phenomenological models, which obtain the coefficients of the model trough experimental data, and type C refers to hybrids of both types [49].

Table F.1: Frequently used hyperelastic models for dielectric elastomers, from [49]

Model	**Type**	**Applicable strain**	**With strain-stiffening**
Neo-Hookean	A	30 % - 40%	No
Arruda-Boyce	A	100 % - 500 %	Yes
Ogden	B	100 % - 400 %	Yes
Yeoh	B	>200 %	No
Gent	C	30 % - 155 %	Yes

These hyperelastic models are input for the constitutive equations as proposed by Suo [59], which describe the behaviour of a DEA subjected to force and voltage:

$$\begin{aligned} \sigma_1 &= \frac{\partial W\left(\lambda_1,\lambda_2,\lambda_3,D\right)}{\lambda_2\lambda_3\partial\lambda_1} - D\cdot E \\ \sigma_2 &= \frac{\partial W\left(\lambda_1,\lambda_2,\lambda_3,D\right)}{\lambda_1\lambda_3\partial\lambda_2} - D\cdot E \\ \sigma_3 &= \frac{\partial W\left(\lambda_1,\lambda_2,\lambda_3,D\right)}{\lambda_1\lambda_2\partial\lambda_3} \\ E &= \frac{\partial W\left(\lambda_1,\lambda_2,\lambda_3,D\right)}{\lambda_1\lambda_2\lambda_3\partial D} \end{aligned} \tag{F.1}$$

where σ_i represents the true stress, λ_i is the stretch ratio, D is the true electric displacement, described as $D = Q/A$ with Q as the electric charges on both electrodes, and $E = U/z$ is the true electric field. For further explanation on the derivation of the constitutive laws in equation F.1 see the detailed demonstration by Wang et al. [49].

Micromechanical model

Neo-Hookean model This model is based on the statistical thermodynamics of cross-linked polymer chains.

$$W_s = \frac{\mu}{2}\left(\lambda_1^2+\lambda_2^2+\lambda_3^2-3\right) \tag{F.2}$$

where μ is the shear modulus (sometimes also denoted by G). This approach leads to a simple model with only one material parameter, which follows the experimental stress-strain behaviour well up to strains of 20 %. After this the strain will approach the stretch limit of the dielectric elastomer and the stiffness will sharply increase and the model is no longer valid [49].

Arruda-Boyce model

$$W_s = \mu \left[\frac{1}{2}\left(I_1 - 3^1\right) + \frac{1}{20n}\left(I_1^2 - 3^2\right) + \frac{11}{1050n^2}\left(I_1^3 - 3^3\right) + \frac{19}{7000n^3}\left(I_1^4 - 3^4\right) + \frac{519}{63750n^4}\left(I_1^5 - 3^5\right) \right] \tag{F.3}$$

where n is a measure of the cross-link density. This model is able to account for the stiffening effect and is therefore valid for larger strains than the Neo-Hookean model.

Phenomenological model

Ogden model This model is a function of the stretch ratios λ_i. Material parameters μ_p and α_p are fitted to experimental data.

$$W_s\left(\lambda_1, \lambda_2, \lambda_3\right) = \sum_{P=1}^{N} \frac{\mu_p}{\alpha_p}\left(\lambda_1^{a_p} + \lambda_2^{\alpha_p} + \lambda_3^{a_p} - 3\right) \tag{F.4}$$

where N is the order of the model and the shear modulus μ follows from $2\mu = \sum_{p=1}^{N} \mu_p \alpha_p$ [52]. This model performs fairly well for electromechanical modeling [49].

Yeoh model This model gives good results when describing the mechanical response of elastomers under large strains [49].

$$W_s\left(\lambda_1, \lambda_2, \lambda_3\right) = C_{10}\left(I_1 - 3\right) + C_{20}\left(I_1 - 3\right)^2 + C_{30}\left(I_1 - 3\right)^3 \tag{F.5}$$

where C_{10}, C_{20} and C_{30} are material parameters obtained from a uniaxial tension experiment and I_1 is the first strain invariant tensor.

Hybrid model

Gent model This model is a hybrid combination because it combines a statistical approach with a material parameter J_{lim}. This is a constant related to the stretch limit, as it is the maximum of the first strain invariant [50].

$$W_s = -\frac{\mu J_{\text{lim}}}{2} \ln\left(1 - \frac{\lambda_1^2 + \lambda_2^2 + \lambda_3^2 - 3}{J_{\text{lim}}}\right) \tag{F.6}$$

where μ is the shear modulus. A a reference, a typical value of J_{lim} for elastomer materials lies around 120 [60]. This model is a popular choice for theoretical analysis due to its mathematical simplicity and it's ability to capture the stiffening of the material at large strains [49].

G

Results of finite element analysis

This appendix contains the results of the FEA variable study. Figure G.1 depicts the variables of the model, as a reference for the tables with results.

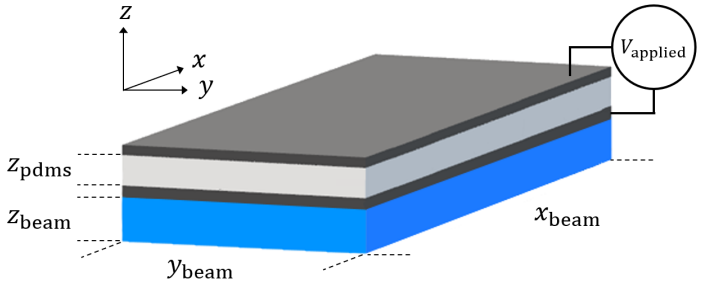

Figure G.1: Schematic drawing of a DEA, indicating the variables of the FEA model

To give a clear overview of all five variables, the results are divided in six tables: for each $V_{applied}$ one table containing the deflection of the actuator in μm and one table where these results are scaled with the value of the benchmark variable set. The benchmark variable set and their corresponding deflection are listed below:

$V_{applied} = 250, 300, 350$ V
$x_{beam} = 5$ mm
$y_{beam} = 1$ mm
$z_{pdms} = 30$ μm
$z_{beam} = 35$ μm

250 V : deflection = 0.013291 μm
300 V : deflection = 0.019134 μm
350 V : deflection = 0.026037 μm

Table G.1: Deflection of a cantilever [μm] actuated at $V_{\text{applied}} = 250$ V, with the benchmark value used in table G.2 in bold

	$V_{\text{applied}} = 250$ V												
	z_{pdms}	5 μm			15 μm			30 μm			45 μm		
z_{beam}	x_{beam} / y_{beam}	1 mm	5 mm	10 mm	1 mm	5 mm	10 mm	1 mm	5 mm	10 mm	1 mm	5 mm	10 mm
10 μm	0.5 mm	0.017457	0.23815	1.1456	0.009291	0.025151	0.08296	0.006303	0.008597	0.021208	0.004287	0.005111	0.010089
	1 mm	0.019216	0.27178	1.6132	0.009031	0.026311	0.091896	0.006238	0.008557	0.021522	0.004332	0.005095	0.009969
	5 mm	0.022422	0.35688	2.2327	0.009226	0.032589	0.10852	0.006261	0.009463	0.023709	0.004355	0.005354	0.010638
20 μm	0.5 mm	0.014369	0.20551	0.88584	0.009391	0.036396	0.13175	0.006423	0.011636	0.035188	0.00439	0.006337	0.016265
	1 mm	0.015069	0.217	0.99048	0.009133	0.037668	0.13781	0.00637	0.011764	0.035833	0.004435	0.006369	0.016403
	5 mm	0.017028	0.27598	1.1986	0.009362	0.047624	0.15897	0.006431	0.013955	0.039937	0.004473	0.00709	0.017838
35 μm	0.5 mm	0.011863	0.13108	0.54223	0.009164	0.033938	0.12576	0.006407	0.013139	0.042005	0.004427	0.007416	0.020769
	1 mm	0.011793	0.13575	0.5683	0.008821	0.034765	0.12902	0.006346	**0.013291**	0.042654	0.004477	0.007444	0.021033
	5 mm	0.012663	0.17039	0.64005	0.008903	0.043482	0.14602	0.00639	0.016088	0.047693	0.00452	0.008696	0.023227
50 μm	0.5 mm	0.011053	0.09165	0.3743	0.009047	0.027646	0.10188	0.006363	0.012479	0.039834	0.004412	0.007529	0.021411
	1 mm	0.010705	0.09437	0.38576	0.008671	0.02813	0.10386	0.006297	0.012577	0.040364	0.00446	0.007556	0.021681
	5 mm	0.011143	0.11809	0.42824	0.008688	0.034712	0.1166	0.006322	0.015009	0.044977	0.004496	0.008828	0.02398

Table G.2: Relative deflection of a cantilever [-] actuated at $V_{applied}$ = 250 V

	$V_{applied}$ = 250 V												
	z_{pdms}	5 μm			15 μm			30 μm			45 μm		
z_{beam}	x_{beam} / y_{beam}	1 mm	5 mm	10 mm	1 mm	5 mm	10 mm	1 mm	5 mm	10 mm	1 mm	5 mm	10 mm
10 μm	0.5 mm	1.31	17.92	86.19	0.70	1.89	6.24	0.47	0.65	1.60	0.32	0.38	0.76
	1 mm	1.45	20.45	121.38	0.68	1.98	6.91	0.47	0.64	1.62	0.33	0.38	0.75
	5 mm	1.69	26.85	167.99	0.69	2.45	8.16	0.47	0.71	1.78	0.33	0.40	0.80
20 μm	0.5 mm	1.08	15.46	66.65	0.71	2.74	9.91	0.48	0.88	2.65	0.33	0.48	1.22
	1 mm	1.13	16.33	74.52	0.69	2.83	10.37	0.48	0.89	2.70	0.33	0.48	1.23
	5 mm	1.28	20.76	90.18	0.70	3.58	11.96	0.48	1.05	3.00	0.34	0.53	1.34
35 μm	0.5 mm	0.89	9.86	40.80	0.69	2.55	9.46	0.48	0.99	3.16	0.33	0.56	1.56
	1 mm	0.89	10.21	42.76	0.66	2.62	9.71	0.48	**1.00**	3.21	0.34	0.56	1.58
	5 mm	0.95	12.82	48.16	0.67	3.27	10.99	0.48	1.21	3.59	0.34	0.65	1.75
50 μm	0.5 mm	0.83	6.90	28.16	0.68	2.08	7.67	0.48	0.94	3.00	0.33	0.57	1.61
	1 mm	0.81	7.10	29.02	0.65	2.12	7.81	0.47	0.95	3.04	0.34	0.57	1.63
	5 mm	0.84	8.88	32.22	0.65	2.61	8.77	0.48	1.13	3.38	0.34	0.66	1.80

Table G.3: Deflection of a cantilever [μm] actuated at $V_{\text{applied}} = 300$ V, with the benchmark value used in table G.4 in bold

	$V_{\text{applied}} = 300$ V												
	z_{pdms}	5 μm			15 μm			30 μm			45 μm		
z_{beam}	x_{beam} / y_{beam}	1 mm	5 mm	10 mm	1 mm	5 mm	10 mm	1 mm	5 mm	10 mm	1 mm	5 mm	10 mm
10 μm	0.5 mm	0.025053	0.34799	1.8095	0.013375	0.035836	0.11449	0.009076	0.012359	0.030235	0.006173	0.007357	0.014488
	1 mm	0.027604	0.41391	2.822	0.013002	0.037814	0.13206	0.008982	0.012311	0.030857	0.006238	0.007335	0.014331
	5 mm	0.032209	0.55177	4.0683	0.013282	0.047119	0.16022	0.009015	0.013629	0.034233	0.00627	0.00771	0.015329
20 μm	0.5 mm	0.020676	0.29855	1.3342	0.01352	0.052218	0.18753	0.009248	0.016738	0.050467	0.006321	0.009122	0.023389
	1 mm	0.021687	0.31887	1.5501	0.013149	0.05422	0.19879	0.009173	0.016932	0.051538	0.006387	0.00917	0.023609
	5 mm	0.02451	0.40702	1.9215	0.013479	0.068733	0.23225	0.00926	0.0201	0.057649	0.006441	0.01021	0.025707
35 μm	0.5 mm	0.017078	0.1899	0.8007	0.013195	0.048804	0.18034	0.009225	0.01891	0.06038	0.006375	0.010676	0.029886
	1 mm	0.016978	0.19744	0.8515	0.0127	0.050061	0.18606	0.009138	**0.019134**	0.061396	0.006447	0.010718	0.030281
	5 mm	0.018231	0.24749	0.95951	0.012819	0.062673	0.21158	0.009201	0.02317	0.068772	0.006509	0.012523	0.033465
50 μm	0.5 mm	0.015912	0.13264	0.54953	0.013026	0.039784	0.1464	0.009162	0.017964	0.057301	0.006353	0.01084	0.030818
	1 mm	0.015413	0.13685	0.57084	0.012485	0.040511	0.14974	0.009067	0.018108	0.058114	0.006423	0.01088	0.031216
	5 mm	0.016042	0.1709	0.63026	0.01251	0.050013	0.16848	0.009103	0.021615	0.064821	0.006475	0.012712	0.034544

Table G.4: Relative deflection of a cantilever [-] actuated at $V_{applied}$ = 300 V

	$V_{applied}$ = 300 V												
	z_{pdms}	5 μm			15 μm			30 μm			45 μm		
z_{beam}	x_{beam} / y_{beam}	1 mm	5 mm	10 mm	1 mm	5 mm	10 mm	1 mm	5 mm	10 mm	1 mm	5 mm	10 mm
10 μm	0.5 mm	1.31	18.19	94.57	0.70	1.87	5.98	0.47	0.65	1.58	0.32	0.38	0.76
	1 mm	1.44	21.63	147.49	0.68	1.98	6.90	0.47	0.64	1.61	0.33	0.38	0.75
	5 mm	1.68	28.84	212.62	0.69	2.46	8.37	0.47	0.71	1.79	0.33	0.40	0.80
20 μm	0.5 mm	1.08	15.60	69.73	0.71	2.73	9.80	0.48	0.87	2.64	0.33	0.48	1.22
	1 mm	1.13	16.67	81.01	0.69	2.83	10.39	0.48	0.88	2.69	0.33	0.48	1.23
	5 mm	1.28	21.27	100.42	0.70	3.59	12.14	0.48	1.05	3.01	0.34	0.53	1.34
35 μm	0.5 mm	0.89	9.92	41.85	0.69	2.55	9.43	0.48	0.99	3.16	0.33	0.56	1.56
	1 mm	0.89	10.32	44.50	0.66	2.62	9.72	0.48	**1.00**	3.21	0.34	0.56	1.58
	5 mm	0.95	12.93	50.15	0.67	3.28	11.06	0.48	1.21	3.59	0.34	0.65	1.75
50 μm	0.5 mm	0.83	6.93	28.72	0.68	2.08	7.65	0.48	0.94	2.99	0.33	0.57	1.61
	1 mm	0.81	7.15	29.83	0.65	2.12	7.83	0.47	0.95	3.04	0.34	0.57	1.63
	5 mm	0.84	8.93	32.94	0.65	2.61	8.81	0.48	1.13	3.39	0.34	0.66	1.81

Table G.5: Deflection of a cantilever [μm] actuated at $V_{\text{applied}} = 350$ V, with the benchmark value used in table G.6 in bold

	$V_{\text{applied}} = 350$ V												
	z_{pdms}	5 μm			15 μm			30 μm			45 μm		
z_{beam}	x_{beam} / y_{beam}	1 mm	5 mm	10 mm	1 mm	5 mm	10 mm	1 mm	5 mm	10 mm	1 mm	5 mm	10 mm
10 μm	0.5 mm	0.033962	0.4802	2.7082	0.0182	0.048158	0.14769	0.012352	0.016789	0.040661	0.008402	0.010009	0.019653
	1 mm	0.037462	0.59915	4.6928	0.017692	0.051346	0.17924	0.012225	0.01674	0.041782	0.008491	0.00998	0.019466
	5 mm	0.043715	0.81178	6.9931	0.018073	0.064438	0.22443	0.01227	0.018553	0.046742	0.008534	0.010494	0.020881
20 μm	0.5 mm	0.028116	0.41013	1.9058	0.018399	0.070762	0.25164	0.012587	0.022754	0.068362	0.008604	0.012411	0.031784
	1 mm	0.0295	0.44412	2.3111	0.017894	0.07376	0.27112	0.012484	0.023034	0.070047	0.008692	0.012479	0.032115
	5 mm	0.033343	0.56942	2.9362	0.018343	0.093798	0.32147	0.012603	0.027367	0.07869	0.008767	0.013898	0.035023
35 μm	0.5 mm	0.023237	0.26021	1.1204	0.017958	0.066318	0.24423	0.012555	0.025723	0.082009	0.008677	0.014528	0.040645
	1 mm	0.023103	0.27183	1.212	0.017285	0.068135	0.25367	0.012438	**0.026037**	0.083525	0.008774	0.014586	0.041206
	5 mm	0.024808	0.34027	1.3671	0.017446	0.0854	0.29009	0.012523	0.031541	0.093758	0.008859	0.017046	0.045578
50 μm	0.5 mm	0.021653	0.18156	0.76432	0.017729	0.054108	0.19877	0.01247	0.024442	0.077896	0.008647	0.014752	0.041925
	1 mm	0.020973	0.18779	0.80141	0.016992	0.055146	0.2041	0.012341	0.024644	0.079081	0.008741	0.014807	0.042483
	5 mm	0.02183	0.23398	0.8797	0.017026	0.068117	0.23024	0.012389	0.029422	0.088315	0.008813	0.017303	0.047037

Table G.6: Relative deflection of a cantilever [-] actuated at $V_{applied}$ = 350 V

	$V_{applied}$ = 350 V												
	z_{pdms}	5 μm			15 μm			30 μm			45 μm		
z_{beam}	x_{beam} / y_{beam}	1 mm	5 mm	10 mm	1 mm	5 mm	10 mm	1 mm	5 mm	10 mm	1 mm	5 mm	10 mm
10 μm	0.5 mm	1.30	18.44	104.01	0.70	1.85	5.67	0.47	0.64	1.56	0.32	0.38	0.75
	1 mm	1.44	23.01	180.24	0.68	1.97	6.88	0.47	0.64	1.60	0.33	0.38	0.75
	5 mm	1.68	31.18	268.58	0.69	2.47	8.62	0.47	0.71	1.80	0.33	0.40	0.80
20 μm	0.5 mm	1.08	15.75	73.20	0.71	2.72	9.66	0.48	0.87	2.63	0.33	0.48	1.22
	1 mm	1.13	17.06	88.76	0.69	2.83	10.41	0.48	0.88	2.69	0.33	0.48	1.23
	5 mm	1.28	21.87	112.77	0.70	3.60	12.35	0.48	1.05	3.02	0.34	0.53	1.35
35 μm	0.5 mm	0.89	9.99	43.03	0.69	2.55	9.38	0.48	0.99	3.15	0.33	0.56	1.56
	1 mm	0.89	10.44	46.55	0.66	2.62	9.74	0.48	**1.00**	3.21	0.34	0.56	1.58
	5 mm	0.95	13.07	52.51	0.67	3.28	11.14	0.48	1.21	3.60	0.34	0.65	1.75
50 μm	0.5 mm	0.83	6.97	29.36	0.68	2.08	7.63	0.48	0.94	2.99	0.33	0.57	1.61
	1 mm	0.81	7.21	30.78	0.65	2.12	7.84	0.47	0.95	3.04	0.34	0.57	1.63
	5 mm	0.84	8.99	33.79	0.65	2.62	8.84	0.48	1.13	3.39	0.34	0.66	1.81